The international journal of science / 11 June 2026

spotlight
Drug discovery

nature



FLAVOUR PROFILES

Early JUNO data capture neutrino oscillations with improved precision

Now trending
Is the hype around peptide drugs backed up by the science?

Proof of concept
How AI use might add up to success for maths and physics

Framework for life
3D structures of protein lattices in mouse egg cells

Vol. 654, No. 8118
£10.00 nature.com



Article

Measurement of reactor neutrino oscillation with the first JUNO data

https://doi.org/10.1038/s41586-026-10538-z

Received: 24 November 2025

Accepted: 14 April 2026

Published online: 10 June 2026

Check for updates

The JUNO Collaboration*✉

Neutrino oscillations (see refs. 1,2 and references therein), a quantum effect manifesting at macroscopic scales, are governed by lepton flavour mixing angles and neutrino mass-squared differences[3] that are fundamental parameters of particle physics, representing phenomena beyond the Standard Model. Precision measurements of these parameters are essential for testing the completeness of the three-flavour framework, determining the mass ordering of neutrinos and probing possible new physics. The Jiangmen Underground Neutrino Observatory (JUNO)[4] is a 20-ktonne liquid-scintillator detector located 52.5 km from multiple reactor cores, designed to resolve the interference pattern of reactor neutrinos with sub-percent precision[5,6]. Here we report, using the first 59.1 days of data collected since detector completion in August 2025, the first simultaneous high-precision determination of two neutrino oscillation parameters, $\sin^2\theta_{12} = 0.3092 \pm 0.0087$ and $\Delta m^2_{21} = (7.50 \pm 0.12) \times 10^{-5}$ eV^2 for the normal mass ordering scenario, improving the precision by a factor of 1.6 relative to the combination of all previous measurements. These results advance the basic understanding of neutrinos, validate the design of the detector and indicate the readiness of JUNO for resolving the neutrino mass ordering with a larger dataset. The rapid achievement with a short exposure highlights the potential of JUNO to push the frontiers of precision neutrino physics and paves the way for its broad scientific programme.

Neutrinos and antineutrinos are fundamental particles that interact by the weak force in the electron ($\nu_e/\bar{\nu}_e$), muon ($\nu_\mu/\bar{\nu}_\mu$) and tau ($\nu_\tau/\bar{\nu}_\tau$) flavours. They propagate as coherent superpositions of the mass eigenstates ν_1, ν_2 and ν_3 with corresponding masses m_1, m_2 and m_3, allowing them to transform from one flavour to another. This phenomenon, known as neutrino oscillation (see refs. 1,2 and references therein) and arising from the mismatch between the flavour and mass eigenstates, is described by three mixing angles (θ_{12}, θ_{23} and θ_{13}), two independent mass-squared differences ($\Delta m^2_{21} \equiv m_2^2 - m_1^2$, $\Delta m^2_{31} \equiv m_3^2 - m_1^2$), and one CP-violating phase. Precision determination of these parameters provides a stringent test of the unitarity of lepton flavour mixing[7,8], validates the three-flavour framework, and constrains explorations of the Majorana nature of neutrinos, the matter–antimatter asymmetry, and the large-scale structure of the universe[3,9].

A global programme using solar, atmospheric, reactor and accelerator neutrinos has yielded increasingly precise determinations of neutrino oscillation parameters. Solar neutrino experiments[10,11] first measured the parameters θ_{12} and Δm^2_{21}, hereafter referred to as the 'solar parameters'. Reactor experiments later confirmed this oscillation pattern[12] and provided precise measurements of Δm^2_{21} (ref. 13). Atmospheric[14] and accelerator[15,16] experiments determined $|\Delta m^2_{31}|$ and θ_{23}, referred to as the 'atmospheric parameters'. Short-baseline reactor experiments established a nonzero θ_{13}, linking the solar and atmospheric sectors[17].

The JUNO experiment was proposed to determine which neutrino mass ordering, normal ($m_1 < m_2 < m_3$) or inverted ($m_3 < m_1 < m_2$), exists in nature[18–22], by detecting electron antineutrinos produced in the β-decays of fission products from nuclear reactors. Determining the neutrino mass ordering hinges on resolving a fine-scale oscillation ripple (driven by Δm^2_{31}) superimposed on a slow, large-amplitude wave (driven by Δm^2_{21}), with the ordering signature encoded in the phase of this fine-scale structure. The JUNO site, located beneath Dashi Hill in Guangdong, China, is shielded by 650 m of rock overburden (about 1,800 m water equivalent) from cosmic radiation. The detector is positioned near the first maximum of the solar-driven oscillations, at an optimized distance of 52.5 km, equidistant from all reactor cores of the Yangjiang and Taishan Nuclear Power Plants[5,22,23]. At this baseline, the interference between oscillation frequencies produces a maximal spectral distortion in the reactor neutrino energy spectrum, from which the oscillation parameters can be precisely extracted. JUNO is a liquid scintillator detector that, thanks to advances in detector size[24] and energy resolution[25], inaugurates a new era of precision in the neutrino sector, with projected sub-percent sensitivity to Δm^2_{21}, Δm^2_{31} and $\sin^2\theta_{12}$ (ref. 6). JUNO also has vast potential[4,23] in astroparticle physics[26–32] and in searches beyond the Standard Model[33–35].

This paper presents the first physics results of JUNO, marking the end of a decade-long effort from the start of construction in 2015 to detector completion in August 2025. Based on 59.1 days of initial data (corresponding to 69 calendar days), our findings showcase the performance of JUNO and yield, to our knowledge, the most precise and simultaneous measurements of solar oscillation parameters Δm^2_{21} and $\sin^2\theta_{12}$, to date. They also establish the foundation for the long-term programme

*A list of authors and their affiliations appears online. ✉e-mail: juno_pub_comm@ihep.ac.cn

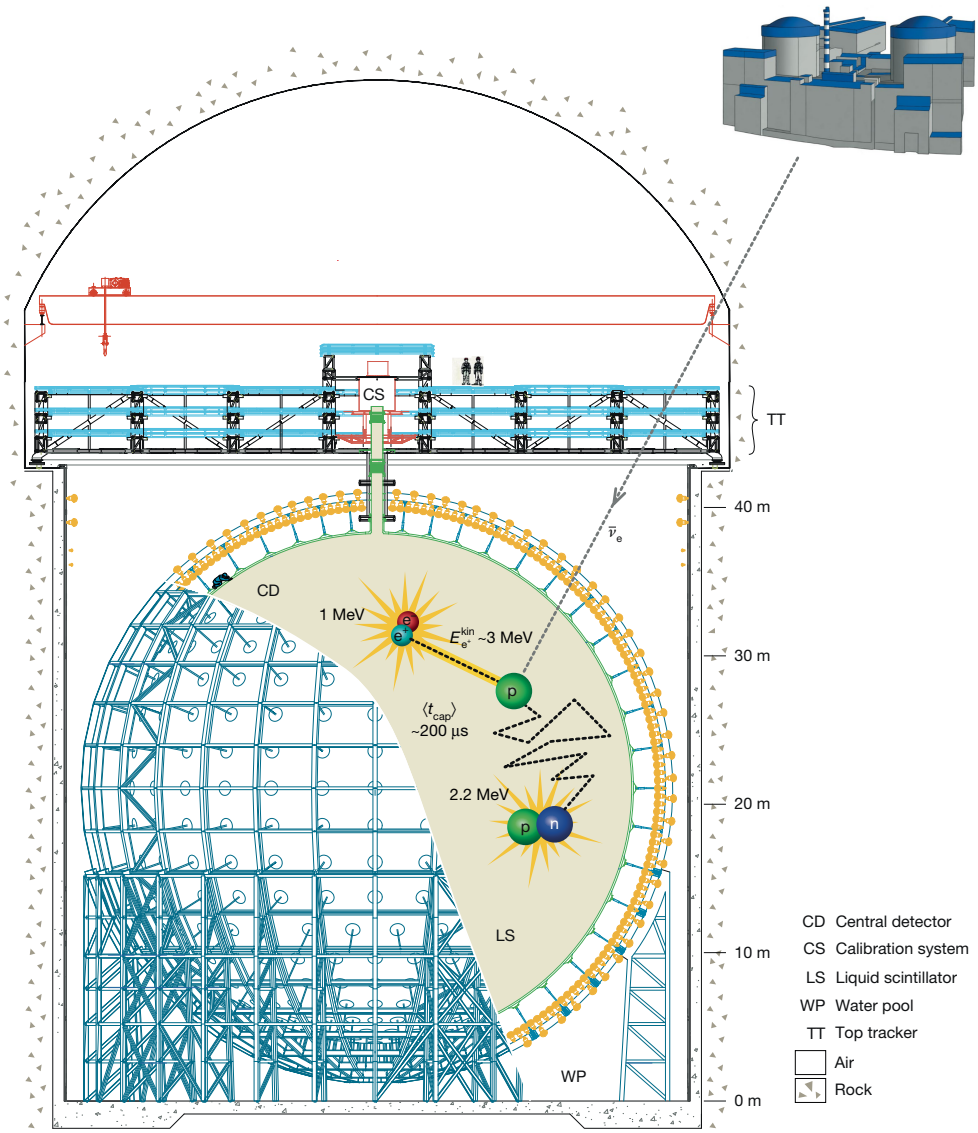


Fig. 1 | JUNO experimental layout. The 20 ktonne liquid scintillator detector is located underground to detect electron antineutrinos from nuclear reactors through inverse β-decay interaction, cartooned inside the detector.

of JUNO to determine the neutrino mass ordering, test the completeness of the three-flavour framework and probe possible new physics.

JUNO experimental setup

JUNO comprises a liquid scintillator (LS) central detector (CD), surrounded by a large water pool (WP), and an external plastic-scintillator top tracker (TT), as shown in Fig. 1. The 20-ktonne LS target is contained within a 17.7-m-radius acrylic vessel, viewed by 17,596 20-inch (4,939 dynode and 12,657 micro-channel plate) and 25,587 three-inch photomultiplier tubes (PMTs)[36], which record the intensity and timing of scintillation light with 78% total geometrical coverage. A high-purity water buffer (≥1.5 m thickness) separates the vessel from the PMTs, whereas an outer water Cherenkov detector, at least 1.55 m thick, shields against radioactivity and tags cosmic muons and their subsequent cosmogenic backgrounds. The TT partially covers the CD to provide a high-purity and high-precision muon sample for evaluating muon-tagging efficiency and tracking precision in the CD.

To resolve the fine oscillation structure necessary for determining the neutrino mass ordering, JUNO is designed to achieve an energy resolution of 3% at 1 MeV (ref. 25), unprecedented for a detector of this scale. This performance requires a correspondingly high light yield so that statistical fluctuations remain sufficiently small. Energy-scale non-linearity, mainly from ionization quenching and Cherenkov light emission, is controlled to sub-percent precision through an extensive calibration programme using radioactive sources, a laser system and two different PMT systems[37].

Further details on the JUNO detector design and instrumentation are provided in Methods and in ref. 36 describing the initial performance results of the JUNO detector.

Data analysis

Reactor neutrinos with energies up to about 11 MeV are identified by inverse beta decay (IBD), $\bar{\nu}_e + p \rightarrow e^+ + n$, where the prompt positron and delayed neutron capture ($\tau \sim 200$ µs) provide distinctive signatures in space, time and energy (Fig. 1). The prompt energy relates to the antineutrino energy through $E_p \approx E_{\bar{\nu}_e} - 0.784$ MeV. Given the 1.8 MeV IBD kinematic threshold[38], the observable E_p spectrum begins at approximately 1 MeV. Oscillation parameters are extracted from characteristic distortions in the E_p spectrum using a multi-step analysis. Events are reconstructed and selected using criteria optimized for high signal

efficiency and strong background suppression. The detector response, linking reconstructed to true energy, is calibrated using both deployed radioactive sources and naturally occurring backgrounds. Residual backgrounds are quantified using control samples or Monte Carlo simulations.

We used data from 26 August 2025 to 2 November 2025 with a live time of 59.1 days. The results, validated across three independent analyses, are consistent. One procedure is presented here, with methodological differences described in the Methods.

Calibration and reconstruction

The light yield, approximately 1,785 photoelectrons (p.e.) per MeV, was calibrated using the neutron capture peak from an ^{241}Am–^{13}C (AmC) source deployed at the detector centre[36]. Event reconstruction uses the PMT waveform information, in which the signal time represents the photon arrival time and the charge corresponds to the integrated signal in p.e. Several likelihood algorithms combining these observables, with corrections accounting for spatial variations derived from the calibration data and natural sources, are used to reconstruct event positions and energies, returning comparable performances. For ^{68}Ge deployed along the z-axis with $|z| < 16.5$ m, the vertex bias is within [−13, +10] cm; meanwhile, the vertex resolution ranges from 13 cm to 27 cm.

The spatio-temporal energy response of the central detector was characterized using multiple calibration sources. The energy scale was calibrated using the 2.223 MeV γ peak from AmC neutron-capture events. Together with the AmC calibrations at the detector centre, high-statistics spallation neutrons enabled daily corrections for temporal variations, resulting in a residual variation of 0.2% that was validated by α decays from ^{214}Po and ^{210}Po. Spatial uniformity of the energy response was primarily evaluated using the neutron-capture peak across the fiducial volume ($R < 16.5$ m). Variations, including both zenith and azimuth angular bins at each radius, shown in Fig. 2a, indicated a residual non-uniformity of around 0.45%. The slight residual discrepancy in energy scale among different neutron samples could result from the limited set of calibration points and muon-induced afterpulses. Figure 2b shows the relative residual energy biases and systematic uncertainties for all monoenergetic sources. The reference energy E_0 is defined as the energy peak at the detector centre for each γ source, and the volume-averaged energy for α decays. Data from ^{68}Ge and ^{214}Po, which are inputs to the likelihood-based energy reconstruction, provided a self-consistency check. The residual temporal and spatial variations in ^{210}Po agreed with both ^{214}Po and neutron capture results. An overall energy-scale uncertainty of 0.5% was assigned and accounted for in the evaluation of the uncertainty in the energy non-linearity model.

Energy scale non-linearity, consisting of scintillator non-linearity and instrumental non-linearity, directly affects the reconstructed antineutrino energy, and therefore the determination of oscillation parameters, see ref. 39. Scintillator non-linearity originates mainly from ionization quenching (Birks's law) and Cherenkov light emission, whereas instrumental non-linearity is caused by residual non-linearity of PMT charge reconstruction. The non-linearity models were constrained by dedicated calibrations at the detector centre with γs covering around 0.5–6 MeV (the reference energies in Fig. 2b) complemented by a continuous β^- spectrum (up to about 14 MeV) and the β^+ spectrum (up to around 2 MeV) from cosmogenic isotopes. This yielded a positron energy non-linearity, known with a precision of 0.6% (Methods), applied in the oscillation fit.

Antineutrino event selection

The IBD signature is identified through the spatio-temporal coincidence between a prompt signal (positron kinetic energy deposition and its annihilation with an electron into two 0.511 MeV γs) and a delayed signal (neutron capture on hydrogen producing a 2.223 MeV γ). This distinctive signature provides strong background rejection while maintaining high signal efficiency.

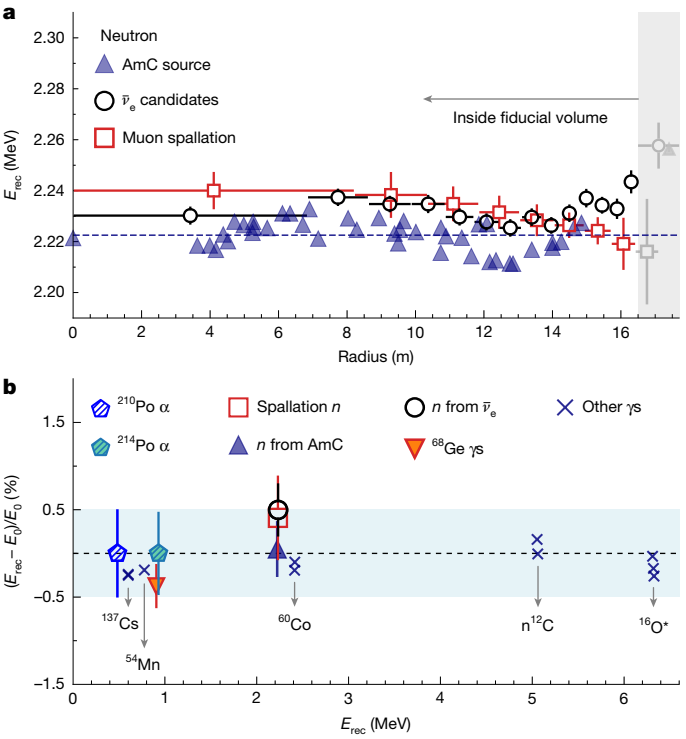


Fig. 2 | JUNO energy scale uncertainty. a, Reconstructed energy E_{rec} of the 2.223 MeV neutron-capture γ peak (dashed line) from AmC sources, $\bar{\nu}_e$ candidates, and spallation neutrons across the full detector volume. **b**, Relative residual energy biases for all monoenergetic sources. The shaded markers represent the sources used as input to the reconstruction. The residuals for the α data (pentagon) are at zero by construction. The error bars for ^{68}Ge, neutrons and α-decays cover the observed residual temporal and spatial variations across the fiducial volume. The crosses denote the measured peaks of individual γ source deployments at different off-centre locations, which have very small statistical uncertainties. The blue band represents the estimated overall systematic uncertainty of ±0.5%.

Reactor neutrino candidates were selected using four principal criteria: spatio-temporal coincidence, a fiducial-volume (FV) cut to suppress external backgrounds, a dedicated muon veto to reject cosmogenic backgrounds and a multiplicity cut to reduce instrumental and multi-particle coincidence backgrounds. Muons were identified with high efficiency (>99.9%) by charge thresholds in both the central detector (about 5 Hz) and the water pool (around 9 Hz). Spallation neutrons were tagged based on energy and timing relative to preceding muons. A temporal veto following muons removed short-lived muon-induced backgrounds, whereas a combined spatio-temporal veto around identified spallation neutrons suppressed long-lived cosmogenic products. The multiplicity cut rejects IBD candidates for which additional energy deposits are observed within a defined time window surrounding the prompt-delayed pair, thereby avoiding ambiguities in event association and suppressing accidental and correlated backgrounds.

The FV cut selects prompt candidate vertices within 16.5 m of the detector centre, reducing contributions from radioactivity at the detector edge and avoiding regions with complex optical behaviour. Regions nearest to the poles of the detector are also excluded because of the complex structure and degraded reconstruction performance. The FV cut efficiency was evaluated from geometrical volume fraction (80.6%) and is validated with uniformly distributed prompt IBD candidates with energies above 3.5 MeV, to exclude contamination from non-homogeneously distributed external backgrounds, and an independent cosmogenic ^{12}B sample with energies above 4 MeV. The residual non-uniformity near the fiducial boundary, evaluated using three independent vertex-reconstruction algorithms, results in

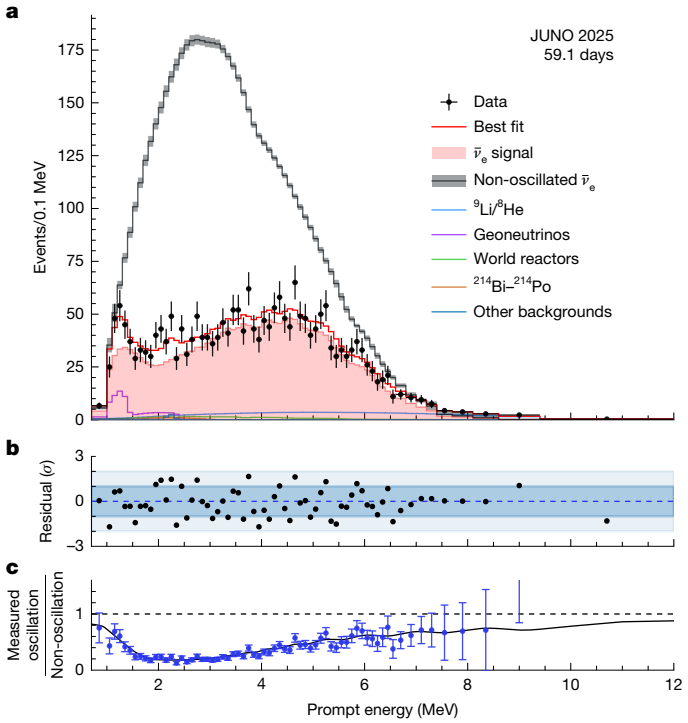


Fig. 3 | Measured energy spectrum of prompt IBD candidates. a, Black points show measured data with statistical error bars, with the red curve indicating the best-fit oscillation model. The red-shaded region represents the expected antineutrino signal. The black solid line represents the non-oscillated reactor neutrino expectation, with the shaded band showing the spectral systematic uncertainty. Backgrounds are indicated by other solid colour lines. **b**, Residuals quantifying the statistical consistency between data and the complete model. **c**, Ratio of the measured oscillated spectrum to non-oscillated prediction.

a relative uncertainty of 1.6%. A separate cross-check based on calibration measurements yields a consistent error estimate. More details are provided in the Methods.

The efficiencies of the remaining selection criteria (muon veto, spallation-neutron veto and multiplicity cut) were determined through a livetime analysis performed by segmenting the detector volume into 10-cm cubes and summing the livetime accumulated in each segment. This segmentation method addresses the complexity arising from overlapping vetoed volumes and their varying veto durations, which preclude a straightforward analytical calculation of the total livetime. Energy selection efficiencies were validated using calibration sources: the prompt-energy threshold with the ^{68}Ge source, and the delayed-energy window by the neutron-capture peak of the AmC source. Temporal and spatial coincidence efficiencies were derived from neutron-capture time distribution and the vertex-separation distribution of the IBD candidates, respectively, and were also verified using AmC sources and Monte Carlo simulations. The efficiency due to the quality cut aimed to remove PMT flashers (spontaneous light emission from PMTs) was evaluated based on physics data such as ^{214}Bi–^{214}Po, IBD and calibration sources, as well as validated by Monte Carlo simulations.

The final data set contains 2,379 identified antineutrino candidates. Their reconstructed prompt energy spectrum is presented in Fig. 3. All selection efficiencies and associated uncertainties are summarized in Table 1. The decomposed background components are also provided in Table 1.

Background evaluation

The main backgrounds for this analysis are represented by cosmogenic ^{9}Li/^{8}He isotopes, geoneutrinos, ^{214}Bi–^{214}Po and antineutrinos from other world reactors. Other minor backgrounds are either strongly suppressed by the selection cuts or intrinsically small. More details are provided in the Methods.

The dominant background that originated from cosmogenic ^{9}Li/^{8}He β–n decays was suppressed using a spallation neutron veto. The total and residual rates were evaluated by fitting the time distribution of candidate events since cosmic muons, before and after application of the spallation neutron veto, respectively. The ^{9}Li/^{8}He ratio was constrained by the measurement from Daya Bay[40]. The dependence of the ^{9}Li/^{8}He rate on visible muon energy was compared with Geant4 simulations, and a systematic rate uncertainty of 35% was assigned to encompass fitting uncertainties and data-simulation discrepancies. A high-purity sample of spallation-neutron-tagged ^{9}Li/^{8}He events enabled spectrum comparison with both calculations based on nuclear databases and a parameterized model from the Daya Bay data[41]. This comparison constrained the spectral shape with 20% bin-to-bin uncorrelated uncertainties. Other long-lived β–n emitters were estimated using FLUKA and Geant4 simulations and found to be negligible.

Geoneutrinos, electron antineutrinos emitted in ^{238}U and ^{232}Th decay chains in the interior of Earth, are indistinguishable from reactor neutrinos on an event-by-event basis. Based on geological crust and mantle models, their predicted flux yields (1.1–2.4) IBD events per day interacting in the LS assuming 100% detection efficiency[28]. Taking the variations across the models, we adopted 1.75 events per day with a 40% uncertainty. To account for discrepancies in spectral models[42,43] and oscillation effects, a 5% bin-to-bin spectral shape uncertainty was

Table 1 | Event selection and backgrounds

Antineutrinos ($\bar{\nu}_e$) candidates summary		
DAQ live time (days)	59.1	
$\bar{\nu}_e$ Candidates	2,379	
Selection efficiencies (%)	ε	σ_{rel}
Fiducial volume	80.6	1.6
PMT flasher rejection	>99.9	Negligible
μ Veto	93.6	Negligible
Multiplicity	97.4	Negligible
Prompt-delayed coincidence	95.1	0.13
Total efficiency (ε_{tot})	69.9	1.6
$\bar{\nu}_e$ signal (cpd[a])		
Without ε_{tot} corrected	33.5 ± 1.7	
With ε_{tot} corrected	47.9 ± 2.6	
Non-oscillated $\bar{\nu}_e$	150.9 ± 2.7	
Backgrounds (cpd)	Pre-fit	Best fit
^{9}Li/^{8}He	4.3 ± 1.4	3.9 ± 0.6
Geoneutrinos	1.2 ± 0.5	1.4 ± 0.4
World reactors	0.88 ± 0.09	0.88 ± 0.09
^{214}Bi–^{214}Po	0.18 ± 0.10	0.20 ± 0.10
^{13}C(α, n)^{16}O	0.04 ± 0.02	0.04 ± 0.02
Fast neutrons	0.02 ± 0.02	0.02 ± 0.02
Double neutrons	0.05 ± 0.05	0.07 ± 0.05
Atmospheric neutrinos	0.08 ± 0.04	0.07 ± 0.04
Accidentals (×10^{-2})	4.9 ± 0.3	4.9 ± 0.3
Total	6.80 ± 1.49	6.63 ± 0.74

The table lists the IBD selection criteria with their respective efficiencies (ε) and relative uncertainties (σ_{rel}), alongside the measured or expected pre-fit and best-fit background rates. The $\bar{\nu}_e$ signal rates were derived both with and without applying the efficiency correction to the observed IBD rate, after background subtraction. The non-oscillated prediction is based on reactor operational data and the flux model described in the Methods. The best-fit values for the backgrounds come from the spectral fit.
[a]cpd, counts per day.

applied to the ^{232}Th and ^{238}U spectra, respectively. Furthermore, a 10% uncertainty was applied to the ^{232}Th-to-^{238}U signal ratio to account for possible compositional variations.

World reactor backgrounds—antineutrinos from distant reactors beyond the primary signal sources—were estimated using operational data from Chinese nuclear plants[44] and the IAEA report[45]. This background contributes to 1.26 IBD events per day at the JUNO site, with 10% rate and 5% bin-to-bin shape uncertainties. The rates for the world reactor and geoneutrino backgrounds in Table 1 are scaled down by the total $\bar{\nu}_e$ selection efficiency.

The β–α cascades from ^{214}Bi–^{214}Po (radon daughters) introduce a correlated background, in which delayed α signals can have reconstructed energies elevated into the neutron capture region, either due to γs from excited ^{214}Po states or to elastic scattering on protons. Other backgrounds (Table 1) were measured or simulated and found to be subdominant (Methods).

Reactor–neutrino signal prediction

Antineutrinos in reactors are produced from β-decays of neutron-rich fission fragments of ^{235}U, ^{238}U, ^{239}Pu and ^{241}Pu. The reactor operational data, especially thermal power, fission fractions and spent fuel information, served as inputs to the flux prediction model. The flux model was decomposed into a component common to JUNO and the Daya Bay experiment[46,47], plus a subdominant term covering their differences, including contributions from Taishan, Yangjiang and other distant reactors. Minor corrections from spent nuclear fuel and non-equilibrium isotopes were also included. More details are given in the Methods.

Spectral fit and results

The observed prompt energy spectrum of IBD candidates, shown in Fig. 3, was compared with a detailed prediction to determine the neutrino oscillation parameters. This prediction incorporated the complete sequence of effects from reactor neutrino production to signal detection (details in the Methods): reactor fluxes evaluated by a semi-model-independent combination of Daya Bay near detector data[46,47] and theoretical models[48,49], baselines from JUNO site to multiple reactors as provided in ref. 5, time-dependent fission fractions, neutrino oscillation, including the matter effects of Earth[50], interaction cross-section[38], detector response and estimated backgrounds (Table 1). The error band on the non-oscillated spectrum in Fig. 3 accounts for all spectral systematics, including the flux constraints from Daya Bay near detector data and the detector response of JUNO.

Systematic uncertainties in the reactor flux prediction, shown in Extended Data Table 1, are dominated by the 1.2% contribution from the Daya Bay reference spectrum[46], followed by the 1% uncertainty in the JUNO target proton number, which is driven by the liquid scintillator volume and hydrogen fraction.

The spectral distortion observed in the prompt-energy spectrum in Fig. 3 was primarily shaped by solar oscillation parameters Δm^2_{21} and $\sin^2\theta_{12}$, with a weaker dependence on Δm^2_{31}. Owing to the limited statistics at present, our oscillation analysis concentrated on determining the solar parameters. We derived the best-fit values and allowed regions using a χ^2 statistic based on the combined Neyman–Pearson (CNP) method[51], which incorporates statistical and systematic uncertainties of both signal and backgrounds as well as two individual constraints on oscillation parameters, Δm^2_{31} and $\sin^2\theta_{13}$ (ref. 41). Leaving Δm^2_{31} unconstrained had a negligible impact (<0.06%) on the results. The variations in the crust density of Earth along the neutrino propagation trajectory were negligible, validating the use of a constant density ($\rho = (2.55 \pm 0.25)$ g cm^{-3}) approximation. The robustness of the results was confirmed through independent analyses using different fitting strategies. A blinding strategy was used to conceal the oscillation parameters throughout the analysis. In particular, reactor operational data, including power and fission fractions, were unblinded only after finalizing the analysis framework.

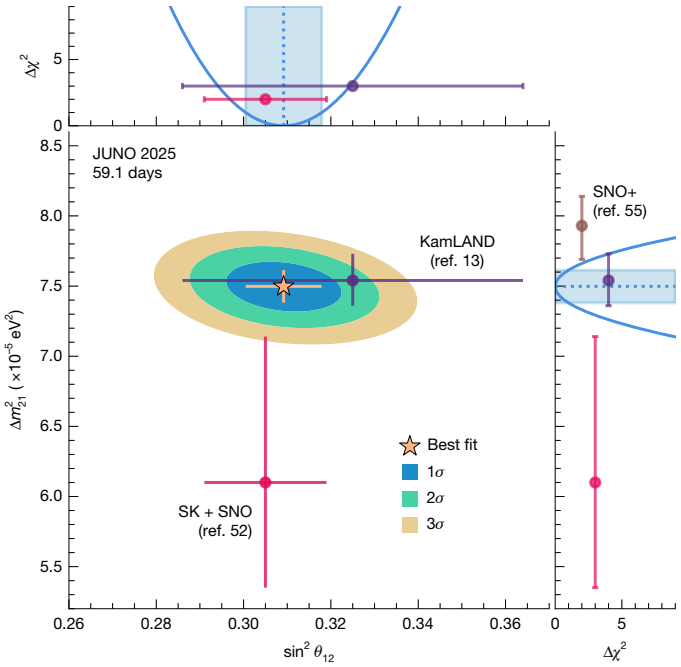


Fig. 4 | Results on solar oscillation parameters. Confidence intervals of $\sin^2\theta_{12}$ and Δm^2_{21} from a spectral fit of measured prompt antineutrino energy spectrum shown in Fig. 3. Shaded elliptically shaped areas correspond to 1σ, 2σ and 3σ confidence regions ($\Delta\chi^2 = 2.30, 6.18, 11.83$, respectively). The top panel provides the one-dimensional $\Delta\chi^2$ for $\sin^2\theta_{12}$ obtained by profiling Δm^2_{21} (blue line) and the blue-shaded region as the corresponding 1σ interval. The right panel is the same, but for Δm^2_{21}, with $\sin^2\theta_{12}$ profiled. The star marks the best fit values of JUNO, and the error bars show their one-dimensional 1σ confidence intervals. Results from other measurements of reactor neutrinos (KamLAND[13] and SNO+[55]) and solar neutrinos (combined Super-Kamiokande (SK) + SNO[52]) are shown for comparison, with the error bars indicating the 1σ range.

The oscillation analysis yielded the following results for the solar parameters for the normal mass ordering scenario:

$$\sin^2\theta_{12} = 0.3092 \pm 0.0087,$$
$$\Delta m^2_{21} = (7.50 \pm 0.12) \times 10^{-5}\ \text{eV}^2.$$

The results for the inverted mass ordering scenario are identical to those for the normal mass ordering at the quoted numerical precision. The allowed regions of oscillation parameters are shown in Fig. 4. (The color scheme is inspired by the Chinese landscape painting: A Panorama of Rivers and Mountains). Consistent with the combination of all previous measurements[13,52], this result improved the precision of both parameters by a factor of 1.6. The current precision of both parameters is statistically limited. The background rate uncertainty constitutes the leading systematic uncertainty for both $\sin^2\theta_{12}$ and Δm^2_{21}. Other important systematic uncertainties arise from the fiducial volume efficiency for $\sin^2\theta_{12}$ and from the reactor antineutrino spectrum shape for Δm^2_{21}, the latter being less sensitive to uncertainties affecting the overall normalization. The uncertainties in the reactor antineutrino rate and shape also contribute to the uncertainty in $\sin^2\theta_{12}$, but with a smaller impact.

Discussion and outlook

JUNO achieves the highest level of precision in the world on the solar oscillation parameters, reducing the uncertainty in Δm^2_{21} to 1.6% (2.5% from KamLAND[13]) and in $\sin^2\theta_{12}$ to 2.81% (4.6% from

Super-Kamiokande + SNO[52] and 5.0% from SNO[53]). Although the current difference between our reactor-based Δm^2_{21} and the solar neutrino value[52] is only at the approximately 1.5σ level, it motivates continued independent probes of this parameter. The upcoming measurement of JUNO of ^{8}B solar neutrinos[31] will provide a direct and competitive measurement of Δm^2_{21} within the same experimental setup.

The precision measurement of solar oscillation parameters at JUNO provides essential experimental input for validating the three-flavour neutrino oscillation model and testing the unitarity of the lepton-flavour-mixing matrix. It also strengthens the physics reach of long-baseline accelerator and atmospheric neutrino experiments in determining the least-known mixing angle, θ_{23}, and in searching for leptonic CP violation. Moreover, it markedly reduces the uncertainties in the effective neutrino mass for neutrinoless double-beta decays, and those in the sum of three neutrino masses for cosmological observations, which are respectively important for probing the Majorana nature of massive neutrinos and the absolute scale of neutrino masses.

The current Δm^2_{31} precision is limited by statistics in the 59.1-day dataset and parameter degeneracies. This precision will improve with increased statistics combined with a model-independent analysis using data from the satellite experiment TAO of JUNO[54]. Overall results confirm that the detector performance, calibration strategy and analysis pipeline perform fully according to design expectations. This provides the first quantitative validation of the ability of JUNO for sub-percent precision oscillation measurements. Building on this validated foundation, further improvements in energy resolution (from enhanced calibration and reconstruction), cosmogenic background rejection (using muon tracks), statistical power (by efficient data-taking and an enlarged fiducial volume) and spectral constraint by TAO together provide a clear path to determining the neutrino mass ordering in future.

Online content

Any methods, additional references, Nature Portfolio reporting summaries, source data, extended data, supplementary information, acknowledgements, peer review information; details of author contributions and competing interests; and statements of data and code availability are available at https://doi.org/10.1038/s41586-026-10538-z.

1. Kajita, T. Nobel lecture: discovery of atmospheric neutrino oscillations. *Rev. Mod. Phys.* **88**, 030501 (2016).
2. McDonald, A. B. Nobel lecture: the Sudbury Neutrino Observatory: observation of flavor change for solar neutrinos. *Rev. Mod. Phys.* **88**, 030502 (2016).
3. Navas, S. et al. Review of particle physics. *Phys. Rev. D* **110**, 030001 (2024).
4. JUNO Collaboration. JUNO physics and detector. *Prog. Part. Nucl. Phys.* **123**, 103927 (2022).
5. Abusleme, A. et al. Potential to identify neutrino mass ordering with reactor antineutrinos at JUNO. *Chin. Phys. C* **49**, 033104 (2025).
6. Abusleme, A. et al. Sub-percent precision measurement of neutrino oscillation parameters with JUNO. *Chin. Phys. C* **46**, 123001 (2022).
7. Pontecorvo, B. Neutrino experiments and the problem of conservation of leptonic charge. *Sov. Phys. JETP* **26**, 984–988 (1968).
8. Maki, Z., Nakagawa, M. & Sakata, S. Remarks on the unified model of elementary particles. *Prog. Theor. Phys.* **28**, 870–880 (1962).
9. Xing, Z.-Z. & Zhou, S. *Neutrinos in Particle Physics, Astronomy and Cosmology*. Advanced Topics in Science and Technology in China (Springer, 2011).
10. Fukuda, S. et al. Solar ^{8}B and hep neutrino measurements from 1258 days of Super-Kamiokande data. *Phys. Rev. Lett.* **86**, 5651–5655 (2001).
11. Ahmad, Q. R. et al. Direct evidence for neutrino flavor transformation from neutral-current interactions in the Sudbury Neutrino Observatory. *Phys. Rev. Lett.* **89**, 011301 (2002).
12. Eguchi, K. et al. First results from KamLAND: evidence for reactor antineutrino disappearance. *Phys. Rev. Lett.* **90**, 021802 (2003).
13. Gando, A. et al. Reactor on-off antineutrino measurement with KamLAND. *Phys. Rev. D* **88**, 033001 (2013).
14. Fukuda, Y. et al. Evidence for oscillation of atmospheric neutrinos. *Phys. Rev. Lett.* **81**, 1562–1567 (1998).
15. Ahn, M. H. et al. Indications of neutrino oscillation in a 250 km long-baseline experiment. *Phys. Rev. Lett.* **90**, 041801 (2003).
16. Michael, D. G. et al. Observation of muon neutrino disappearance with the MINOS detectors in the NuMI neutrino beam. *Phys. Rev. Lett.* **97**, 191801 (2006).
17. An, F. P. et al. Observation of electron-antineutrino disappearance at Daya Bay. *Phys. Rev. Lett.* **108**, 171803 (2012).
18. Petcov, S. & Piai, M. The LMA MSW solution of the solar neutrino problem, inverted neutrino mass hierarchy and reactor neutrino experiments. *Phys. Lett. B* **533**, 94–106 (2002).
19. Learned, J. G., Dye, S. T., Pakvasa, S. & Svoboda, R. C. Determination of neutrino mass hierarchy and θ_{13} with a remote detector of reactor antineutrinos. *Phys. Rev. D* **78**, 071302 (2008).
20. Zhan, L., Wang, Y., Cao, J. & Wen, L. Determination of the neutrino mass hierarchy at an intermediate baseline. *Phys. Rev. D* **78**, 111103(R) (2008).
21. Zhan, L., Wang, Y., Cao, J. & Wen, L. Experimental requirements to determine the neutrino mass hierarchy using reactor neutrinos. *Phys. Rev. D* **79**, 073007 (2009).
22. Li, Y.-F., Cao, J., Wang, Y. & Zhan, L. Unambiguous determination of the neutrino mass hierarchy using reactor neutrinos. *Phys. Rev. D* **88**, 013008 (2013).
23. An, F. et al. Neutrino physics with JUNO. *J. Phys. G Nucl. Part. Phys.* **43**, 030401 (2016).
24. Abusleme, A. et al. The design and technology development of the JUNO central detector. *Eur. Phys. J. Plus* **139**, 1128 (2024).
25. Abusleme, A. et al. Prediction of energy resolution in the JUNO experiment. *Chin. Phys. C* **49**, 013003 (2025).
26. Abusleme, A. et al. Real-time monitoring for the next core-collapse supernova in JUNO. *J. Cosmol. Astropart. Phys.* **01**, 057 (2024).
27. Abusleme, A. et al. Prospects for detecting the diffuse supernova neutrino background with JUNO. *J. Cosmol. Astropart. Phys.* **10**, 033 (2022).
28. Li, Y.-F. Prospects for geoneutrino detection with JUNO. *Chin. Phys. C* https://doi.org/10.1088/1674-1137/ae457d (2026).
29. Abusleme, A. et al. JUNO sensitivity to low energy atmospheric neutrino spectra. *Eur. Phys. J. C* **81**, 887 (2021).
30. Abusleme, A. et al. JUNO sensitivity to ^{7}Be, *pep*, and CNO solar neutrinos. *J. Cosmol. Astropart. Phys.* **10**, 022 (2023).
31. Abusleme, A. et al. Feasibility and physics potential of detecting ^{8}B solar neutrinos at JUNO. *Chin. Phys. C* **45**, 023004 (2021).
32. Zhao, J. et al. Model-independent approach of the JUNO ^{8}B solar neutrino program. *Astrophys. J.* **965**, 122 (2024).
33. Abusleme, A. et al. JUNO sensitivity on proton decay $p \to \overline{\nu}K^+$ searches. *Chin. Phys. C* **47**, 113002 (2023).
34. Abusleme, A. et al. JUNO sensitivity to the annihilation of MeV dark matter in the galactic halo. *J. Cosmol. Astropart. Phys.* **09**, 001 (2023).
35. JUNO Collaboration. JUNO sensitivity to invisible decay modes of neutrons. *Eur. Phys. J. C* **85**, 5 (2025).
36. Abusleme, A. et al. Initial performance results of the JUNO detector. *Chin. Phys. C* **50**, 043001 (2026)
37. Abusleme, A. et al. Calibration strategy of the JUNO experiment. *J. High Energy Phys.* **03**, 004 (2021).
38. Vogel, P. & Beacom, J. F. Angular distribution of neutron inverse beta decay, $\overline{\nu}_e + p \to e^+ + n$. *Phys. Rev. D* **60**, 053003 (1999).
39. Adey, D. et al. A high precision calibration of the nonlinear energy response at Daya Bay. *Nucl. Instrum. Methods Phys. Res. A* **940**, 230–242 (2019).
40. An, F. P. et al. First measurement of the yield of ^{8}He isotopes produced in liquid scintillator by cosmic-ray muons at Daya Bay. *Phys. Rev. D* **110**, L011101 (2024).
41. An, F. P. et al. Precision measurement of reactor antineutrino oscillation at kilometer-scale baselines by Daya Bay. *Phys. Rev. Lett.* **130**, 161802 (2023).
42. Enomoto, S. *Geoneutrino Spectrum and Luminosity*. https://www.awa.tohoku.ac.jp/~sanshiro/research/geoneutrino/spectrum/ (2006).
43. Li, Y.-F. & Xin, Z. New calculation of the geo-neutrino energy spectrum and its implication. Preprint at https://arxiv.org/abs/2412.07711 (2024).
44. China Nuclear Energy Association. *National Nuclear Power Status Reports 2025* https://m.china-nea.cn/site/content/50357.html (CNEA, 2025).
45. IAEA. *Operating Experience with Nuclear Power Stations in Member States 2025 Edition*. IAEA/OPEX/2025. https://www.iaea.org/publications/15944 (2025).
46. An, F. P. et al. Comprehensive measurement of the reactor antineutrino spectrum and flux at Daya Bay. *Phys. Rev. Lett.* **134**, 201802 (2025).
47. Daya Bay Collaboration. Full data release of the Daya Bay reactor neutrino experiment. v1.0.0. *Zenodo* https://doi.org/10.5281/zenodo.17587229 (2025).
48. Huber, P. Determination of antineutrino spectra from nuclear reactors. *Phys. Rev. C* **84**, 024617 (2011).
49. Mueller, Th. A. et al. Improved predictions of reactor antineutrino spectra. *Phys. Rev. C* **83**, 054615 (2011).
50. Li, Y., Wang, Y. & Xing, Z. Terrestrial matter effects on reactor antineutrino oscillations at JUNO or RENO-50: how small is small? *Chin. Phys. C* **40**, 091001 (2016).
51. Ji, X., Gu, W., Qian, X., Wei, H. & Zhang, C. Combined Neyman–Pearson chi-square: an improved approximation to the Poisson-likelihood chi-square. *Nucl. Instrum. Meth. A* **961**, 163677 (2020).
52. Abe, K. et al. Solar neutrino measurements using the full data period of Super-Kamiokande-IV. *Phys. Rev. D* **109**, 092001 (2024).
53. Aharmim, B. et al. Combined analysis of all three phases of solar neutrino data from the Sudbury Neutrino Observatory. *Phys. Rev. C* **88**, 025501 (2013).
54. Abusleme, A. et al. TAO conceptual design report: a precision measurement of the reactor antineutrino spectrum with sub-percent energy resolution. Preprint at https://arxiv.org/abs/2005.08745 (2020).
55. Abreu, M. et al. Measurement of reactor antineutrino oscillation at SNO+. *Phys. Rev. Lett.* **135**, 121801 (2025).

Publisher's note Springer Nature remains neutral with regard to jurisdictional claims in published maps and institutional affiliations.

Springer Nature or its licensor (e.g. a society or other partner) holds exclusive rights to this article under a publishing agreement with the author(s) or other rightsholder(s); author self-archiving of the accepted manuscript version of this article is solely governed by the terms of such publishing agreement and applicable law.

© The Author(s), under exclusive licence to Springer Nature Limited 2026

The JUNO Collaboration

Angel Abusleme[1], Thomas Adam[2], Kai Adamowicz[3], David Adey[4], Shakeel Ahmad[5], Rizwan Ahmed[5], Timo Ahola[6], Sebastiano Aiello[7], Fengpeng An[8], Guangpeng An[4], Costas Andreopoulos[9], Giuseppe Andronico[7], João Pedro Athayde Marcondes de André[2], Nikolay Anfimov[10], Vito Antonelli[11], Tatiana Antoshkina[10], Burin Asavapibhop[12], Didier Auguste[13], Margherita Buizza Avanzini[14], Andrej Babic[15], Jingzhi Bai[4,85], Weidong Bai[8], Nikita Balashov[10], Roberto Barbera[7], Andrea Barresi[16], Davide Basilico[11], Eric Baussan[2], Beatrice Bellantonio[11], Marco Bellato[17], JeanLuc Beney[18], Marco Beretta[11], Antonio Bergnoli[17], Enrico Bernieri[19], Nikita Bessonov[10], David Biaré[10], Daniel Bick[20], Lukas Bieger[21], Svetlana Biktemerova[10], Thilo Birkenfeld[3], David Blum[21], Simon Blyth[4], Sara Boarin[16], Manuel Boehles[22], Anastasia Bolshakova[10], Mathieu Bongrand[18], Aurélie Bonhomme[2], Clément Bordereau[23,24], Matteo Borghesi[16], Augusto Brigatti[11], Timothee Brugiere[2], Riccardo Brugnera[25], Riccardo Bruno[7], Jonas Buchholz[24,18], Antonio Budano[19], Max Buesken[3], Mario Buscemi[7], Severino Bussino[19], Jose Busto[26], Ilya Butorov[10], Marcel Büchner[22], Anatael Cabrera[13], Barbara Caccianiga[11], Boshuai Cai[8], Hao Cai[27], Xiao Cai[4], Yanke Cai[4], Yi-zhou Cai[28], Zhiyan Cai[4], Stéphane Callier[24], Steven Calvez[18], Antonio Cammi[29], Agustin Campeny[30], Dechang Cai[31], Chuanya Cao[4], Dewen Cao[28], Guofu Cao[4], Jun Cao[4,32], Yaoqi Cao[33,9], Rossella Caruso[7], Aurelio Caslini[11], Cédric Cerna[24], Vanessa Cerrone[25], Daniele Cesini[7], Chi Chan[34], Jinfan Chang[4], Yun Chang[35], Milo Charavet[20], Tim Charissé[36,22], Auttakit Chatrabhuti[12], Chao Chen[4], Guoming Chen[37], Haitao Chen[4], Haotian Chen[4], Jiahui Chen[8], Jian Chen[8], Jing Chen[8], Junyou Chen[37], Lihao Chen[8], Mali Chen[4], Mingming Chen[4], Pingping Chen[38], Po-An Chen[23], Quanyou Chen[39], Shaomin Chen[40], Shenjian Chen[28], Shi Chen[41], Shiqiang Chen[28], Sisi Chen[4], Xin Chen[28,4], Xuan Chen[4], Xurong Chen[42], Yi-Wen Chen[34], Yiming Chen[4], Yixue Chen[43], Yu Chen[8], Ze Chen[36,22], Zelin Chen[28,4], Zhang Chen[4], Zhangming Chen[44], Zhiyuan Chen[4,45], Zhongchang Chen[46], Zikang Chen[8], Brian Cheng[47], Jie Cheng[43], Yaping Cheng[48], Yu Chin Cheng[23], Zhaokan Cheng[42], Alexander Chepurnov[49,50], Alexey Chetverikov[10], Davide Chiesa[16], Pietro Chimenti[51], Yen-Ting Chin[23], Pin-Jung Chiu[23], Po-Lin Chou[34], Ziliang Chu[4], Artem Chukanov[10], Neetu Raj Singh Chundawat[4,45], Anna Chuvashova[10], Gérard Claverie[24], Catia Clementi[52], Barbara Clerbaux[53], Claudio Coletta[16], Marta Colomer Molla[53], Flavio Dal Corso[17], Daniele Corti[17], Salvatore Costa[7], Simon Csakli[54], Chenyang Cui[4], Shanshan Cui[4], Lorenzo Vincenzo D'Auria[25], Olivia Dalager[47], Jaydeep Datta[53], Luis Delgadillo Franco[4,45], Jiawei Deng[27], Zhi Deng[40], Ziyan Deng[4], Wilfried Depnering[22], Hanna Didenko[55], Xiaoyu Ding[39], Xuefeng Ding[4], Yayun Ding[4], Bayu Dirgantara[56], Carsten Dittrich[54], Sergey Dmitrievsky[10], David Doerflinger[54], Tadeas Dohnal[55], Maria Dolgareva[10], Dmitry Dolzhikov[10], Chuanshi Dong[4], Haojie Dong[4], Jianmeng Dong[40], Lan Dong[4], Damien Dornic[26], Evgeny Doroshkevich[50], Wei Dou[40], Marcos Dracos[2], Olivier Drapier[14], Tobias Drohmann[54,85], Frédéric Druillole[24], Ran Du[4], Shuxian Du[57], Yujie Duan[27], Katherine Dugas[47], Stefano Dusini[17], Hongyue Duyang[39], Martin Dvorak[55], Jessica Eck[21], Timo Enqvist[6], Heike Enzmann[22], Andrea Fabbri[19], Ulrike Fahrendholz[54], Lukas Fajt[15], Donghua Fan[58], Lei Fan[4], Liangqianjin Fan[4], Can Fang[37], Jian Fang[4], Wenxing Fang[4], Marco Fargetta[7], Elia Stanescu Farilla[19], Anna Fatkina[10], Laurent Favart[53], Dmitry Fedoseev[10], Zhengyong Fei[4], Franz von Feilitzsch[54], Vladko Fekete[15], Li-Cheng Feng[34], Qichun Feng[59], Shaoting Feng[46], Giovanni Ferrante[16], Federico Ferraro[11], Daniela Fetzer[22], Giovanni Fiorentini[60], Andrey Formozov[11], Marcellin Fotzé[2], Amélie Fournier[24], Sabrina Franke[54], Arran Freegard[44], Florian Fritsch[2], Ying Fu[4,45], Haonan Gan[61], Feng Gao[53,3], Ruixuan Gao[8], Ruohan Gao[62], Shijiao Gao[54], Alberto Garfagnini[25], Gerard Gaudiot[2], Arsenii Gavrikov[25], Raphaël Gazzini[24], Christoph Genster[63,3], Diwash Ghimire[44], Marco Giammarchi[11], Agnese Giaz[29], Gianfranco Giordano[64,85], Nunzio Giudice[7], Franco Giuliani[44], Alexandre S. Göttel[63,3], Maxim Gonchar[10], Guanda Gong[4,45], Guanghua Gong[40], Hui Gong[40], Michel Gonin[14], Oleg Gorchakov[10], Yuri Gornushkin[10], Marco Grassi[25], Christian Grewing[65], Maxim Gromov[49,10], Vasily Gromov[10], Minhao Gu[4], Xiaofei Gu[57], Yu Gu[66], Mengyun Guan[4], Yuduo Guan[4], Nunzio Guardone[7], Rosa Maria Guizzetti[25], Cong Guo[4], Jingyuan Guo[8], Wanlei Guo[4], Yuhang Guo[67,4], Paul Hackspacher[22], Caren Hagner[20], Hechong Han[4], Ran Han[43], Xiao Han[4], Yang Han[8], Ziguo Han[4], Chuanhui Hao[40], Jiajun Hao[4], Vidhya Thara Hariharan[20], JinCheng He[43], Jinhong He[27], Miao He[4], Mingtao He[31], Wei He[4], Xinhai He[4], Ziou He[33,9], Tobias Heinz[21], Dominikus Hellgartner[54], Patrick Hellmuth[24], Shilin Heng[57], Yuekun Heng[4], Rafael Herrera[30], Daojin Hong[37], YuenKeung Hor[8], Shaojing Hou[4], Zhilong Hou[4], Fatima Houria[11], Yee Hsiung[23], Bei-Zhen Hu[68], Hang Hu[8], Hao Hu[4], Jianrun Hu[8], Jun Hu[4], Peng Hu[4], Tao Hu[4], Wei Hu[4], Yuxiang Hu[4], Zhuojun Hu[8], Chunhao Huang[8], Guihong Huang[58], Hanyu Huang[44], Hexiang Huang[4], Jinhao Huang[4], Junlin Huang[66], Junting Huang[44], Kairui Huang[4], Kaixuan Huang[8], Qinhua Huang[2,14], Shengheng Huang[58], Tao Huang[8], Wenhao Huang[39], Xiaozhong Huang[28], Xin Huang[4], Xingtao Huang[39], Yongbo Huang[37], Lian-Chen Huang[69], Jiaqi Hui[44], Lei Huo[59], Cédric Huss[24], Safeer Hussain[5], Leonard Imbert[18], Antonio Insolia[7], Ara Ioannisian[70], Daniel Ioannisyan[70], Ammad Ul Islam[19], Roberto Isocrate[17], Adrienne Jacobi[47], Arshak Jafar[22], Beatrice Jelmini[25], Kuo-Lun Jen[34], Ignacio Jeria[1], Soeren Jetter[4], Xiangpan Ji[71], Xiaolu Ji[4], Xingzhao Ji[8], Huihui Jia[71], Junji Jia[27], Yi Jia[4], Cailian Jiang[28], Chengbo Jiang[43], Guangzheng Jiang[72], Junjie Jiang[44], Wei Jiang[4], Xiaoshan Jiang[4], Xiaozhao Jiang[4], Yijian Jiang[43], Yixuan Jiang[4], Yue Jiang[59], Ruyi Jin[4], Shuzhu Jin[4], Xiaoping Jing[4], Cécile Jollet[24], Liam Jones[9,33], Jari Joutsenvaara[6], Sirichok Jungthawan[56], Philipp Kampmann[36], Markus Kaiser[20], Leonidas Kalousis[2], Bowen Kan[4], Li Kang[38], Michael Karagounis[65], Rebin Karaparambil[2], Matej Karas[15], Narine Kazarian[70], Amir Khan[8], Amina Khatun[53,15], Khanchai Khosonthongkee[56], Florian Kiel[3], Patrick Kinz[34], Denis Korablev[10], Konstantin Kouzakov[49], Alexey Krasnoperov[10], Zinovy Krumshteyn[10,85], Andre Kruth[65], Tim Kuhlbusch[3], Sergey Kuleshov[30], Sindhujha Kumaran[47], Chun-Hao Kuo[69], Nikolay Kutovskiy[10], Pasi Kuusiniemi[6], Loïc Labit[2], Tobias Lachenmaier[21], Haojing Lai[44], ToUyen LamThi[34], Philipp Landgraf[54], Cecilia Landini[11], Lorenzo Lastrucci[25], Fedor Lazarev[49], Sébastien Leblanc[24], Victor Lebrin[18], Matthieu Lecocq[24], Priscilla Lecomte[2], Frederic Lefevre[18], Liping Lei[40], Ruiting Lei[38], Xiangcui Lei[4], Rupert Leitner[55], Petr Lenskii[10], Jason Leung[34], Bo Li[4], Chao Li[39], Daozheng Li[4], Demin Li[57], Dian Li[4], Fei Li[4], Fule Li[40], Gaoshuang Li[57,4], Gaosong Li[4], Haitao Li[8], Hongjian Li[4], Huang Li[4], Huiling Li[39], Jiajun Li[8], Jiaqi Li[8], Jin Li[4], Kaijie Li[8], Meiou Li[58], Mengzhao Li[4], Min Li[2], Nan Li[73], Qingjiang Li[73], Quanlin Li[4], Ruhui Li[4], Rui Li[44], Shanfeng Li[38], Shuaijie Li[8], Shuo Li[28], Tao Li[8], Teng Li[39], Weidong Li[4,41], Weiguo Li[4,85], Xiaomei Li[74], Xiaonan Li[45,4], Xiwen Li[4], Xinying Li[71], Yang Li[4], Yawen Li[4], Yi Li[38], Yichen Li[4], Yifan Li[4], Yingke Li[37], Yuanxia Li[4], Yufeng Li[4], Zepeng Li[4], Zhaohan Li[4], Zhibing Li[8], Zhiwei Li[48], Zi-Ming Li[57], Ziyuan Li[8], Zonghai Li[27], An-An Liang[34], Jing Liang[4], Jingjing Liang[37], Jiajun Liao[8], Minghua Liao[8], Yilin Liao[44], Yuzhong Liao[61], Daniel Liebau[65], Ayut Limphirat[56], Sukit Limpijumnong[56], Bo-Chun Lin[34], Guey-Lin Lin[34], Jiming Lin[31], Shengxin Lin[38], Tao Lin[4], Xianhao Lin[28], Xingyi Lin[37], Yen-Hsun Lin[34], Jiacheng Ling[8], Jiajie Ling[8], Xin Ling[4], Ivano Lippi[17], Caimei Liu[4], Fang Liu[43], Fengcheng Liu[43], Gang Liu[4], Haidong Liu[57], Haotian Liu[27], Hongbang Liu[37], Hongjuan Liu[75], Hongtao Liu[8], Hongyang Liu[4], Hu Liu[8], Hui Liu[66], Jianglai Liu[44,76], Jianli Liu[59], Jiaxi Liu[4], Jin'gao Liu[62], Jinchang Liu[4], Jinyan Liu[71], Kainan Liu[58], Lei Liu[4], Libing Liu[4], Mengchao Liu[4], Menglan Liu[8], Min Liu[75], Qishan Liu[4], Qian Liu[41], Qin Liu[77], Runxuan Liu[36,3], Shenghui Liu[4], Shuangyu Liu[4], Shubing Liu[4], Shulin Liu[4], Wanjin Liu[4], Xiaowei Liu[8], Ximing Liu[71], Xinkang Liu[39], Xiwen Liu[37], Xuewei Liu[40], Yan Liu[4], Yankai Liu[67], Yin Liu[39], Yiqi Liu[40], Yuanyuan Liu[71], Yuexiang Liu[4], Yunzhe Liu[4], Zhen Liu[4], Zhipeng Liu[4], Zhuo Liu[4], Domenico Lo Presti[7], Salvatore Loffredo[19], Lorenzo Loi[29], Paolo Lombardi[11], Claudio Lombardo[7], Yongbing Long[58], Fabio Longhitano[7], Kai Loo[6], Sebastian Lorenz[20,22], Selma Conforti Di Lorenzo[24], Chuan Lu[61], Fan Lu[43], Haoqi Lu[4], Jiashu Lu[4], Junguang Lu[4], Meishu Lu[54], Peizhi Lu[8], Shuxiang Lu[57], Xianghui Lu[31], Xianguo Lu[33], Xiaoxu Lu[4], Xiaoying Lu[4], Bayarto Lubsandorzhiev[50], Sultim Lubsandorzhiev[50], Livia Ludhova[36,22], Arslan Lukanov[50], Daibin Luo[4], Fengjiao Luo[75], Guang Luo[8], Jianyi Luo[58], Pengwei Luo[8], Shu Luo[78], Tao Luo[4], Wuming Luo[4], Xiaojie Luo[4], Xiaolan Luo[4], Zhipeng Lv[67], Vladimir Lyashuk[50], Bangzheng Ma[39], Bing Ma[57], Na Ma[4], Qiumei Ma[4], Si Ma[4], Wing Yan Ma[39], Xiaoyan Ma[4], Xubo Ma[43], Santi Maensiri[56], Jingyu Mai[8], Romain Maisonobe[18], Marco Malabarba[36,22], Yury Malyshkin[36,22], Roberto Carlos Mandujano[47], Fabio Mantovani[60], Xin Mao[48], Yajun Mao[79], Stefano M. Mari[19], Cristina Martellini[19], Agnese Martini[64], Jacques Martino[18], Johann Martyn[22], Matthias Mayer[54], Davit Mayilyan[70], Worawat Meevasana[56], Artur Meinusch[22], Qingru Meng[57], Yue Meng[44], Anita Meraviglia[36,3], Anselmo Meregaglia[24], Emanuela Meroni[11], David Meyhöfer[20], Jian Min[4], Lino Miramonti[11], Nikhil Mohan[36,3], Salvatore Monforte[7], Paolo Montini[19], Michele Montuschi[60], Nikolay Morozov[10], Iwan Morton-Blake[76], Xiangyi Mu[4], Pavithra Muralidharan[65], Lakshmi Murgod[4,45], Axel Müller[21], Thomas Mueller[14], Massimiliano Nastasi[16], Dmitry V. Naumov[10], Elena Naumova[10], Diana Navas-Nicolas[13], Igor Nemchenok[10], Elisabeth Neuerburg[3], VanHung Nguyen[34], Dennis Nielinger[65], Alexey Nikolaev[49], Feipeng Ning[4], Zhe Ning[4], Yujie Niu[4], Stepan Novikov[10], Hiroshi Nunokawa[80], Lothar Oberauer[54], Juan Pedro Ochoa-Ricoux[47,30], Samantha Cantu Olea[47], Sebastian Olivares[81], Alexander Olshevskiy[10], Domizia Orestano[19], Fausto Ortica[52], Rainer Othegraven[22], Yifei Pan[8], Alessandro Paoloni[64], Nina Parkalian[65], George Parker[22], Sergio Parmeggiano[11], Achilleas Patsias[3], Teerapat Payupol[12], Viktor Pec[55], Davide Pedretti[17], Yatian Pei[4], Luca Pelicci[11], Nicomede Pelliccia[52], Anguo Peng[75], Haiping Peng[77], Yu Peng[4], Zhaoyuan Peng[4], Elisa Percalli[11], Willy Perrin[2], Frédéric Perrot[24], Pierre-Alexandre Petitjean[53], Fabrizio Petrucci[19], Min Pi[27], Oliver Pilarczyk[22], Ruben Pompilio[11], Artyom Popov[49], Pascal Poussot[2], Stefano Pozzi[16], Wathan Pratumwan[56], Ezio Previtali[16], Sabrina Prummer[54], Fazhi Qi[4], Ming Qi[28], Xiaohui Qi[4], Sen Qian[4], Xiaohui Qian[4], Zhen Qian[8], Liqing Qin[4], Zhonghua Qin[4], Shoukang Qiu[75], Manhao Qu[57], Zhenning Qu[4], Muhammad Usman Rajput[5], Shivani Ramachandran[3], Gioacchino Ranucci[11], Neill Raper[8], Reem Rasheed[24], Thomas Raymond[2], Alessandra Re[11], Henning Rebber[20], Abdel Rebii[24], Bin Ren[38], Shanjun Ren[4], Yuhan Ren[4], Andrea Rendina[7], Cristobal Morales Reveco[36,3,22], Taras Rezinko[10], Barbara Ricci[60], Luis Felipe Piñeres Rico[2], Mariam Rifai[36,3,22], Markus Robens[65], Mathieu Roche[24], Narongkiat Rodphai[4,12], Fernanda de Faria Rodrigues[4], Lars Rohwer[20], Aldo Romani[52], Vincent Rompel[54], Bedřich Roskovec[55], Xiangdong Ruan[37], Xichao Ruan[74], Peter Rudakov[49], Saroj Rujirawat[56], Arseniy Rybnikov[10], Andrey Sadovsky[10,85], Sahar Safari[22], Giuseppe Salamanna[19], Deshan Sandanayake[2], Simone Sanfilippo[19], Anut Sangka[82], Nuanwan Sanguansak[56], Ujwal Santhosh[36,22], Giuseppe Sava[7], Utane Sawangwit[82], Julia Sawatzki[54], Michaela Schever[3], Jacky Schuler[2], Cédric Schwab[2], Konstantin Schweizer[54], Dmitry Selivanov[10], Alexandr Selyunin[10], Andrea Serafini[17], Giulio Settanta[63], Mariangela Settimo[18], Muhammad Ikram Shahzad[5], Yanjun Shan[83], Junyu Shao[4], Zhuang Shao[67], Anurag Sharma[21], Vladislav Sharov[10], Arina Shaydurova[10], Wei Shen[4], Gang Shi[40], Hangyu Shi[8], Hexi Shi[36], Jingyan Shi[4], Yanan Shi[4], Yongjiu Shi[40], Yuan Shi[4], Dmitrii Shpotya[10], Yike Shu[4], Yuhan Shu[4], She Shuai[57], Vitaly Shutov[10], Andrey Sidorenkov[50,4], Randhir Singh[4,45], Apeksha Singhal[36], Chiara Sirignano[25], Jaruchit Siripak[56], Monica Sisti[16], Maciej Slupecki[6], Mikhail Smirnov[20], Oleg Smirnov[10], Thiago Sogo-Bezerra[18], Michael Soiron[3], Sergey Sokolov[10], Julanan Songwadhana[56], Boonrucksar Soonthornthum[82], Felix Sorgenfrei[20], Albert Sotnikov[10], Mario Spinetti[64], Warintorn Sreethawong[56], Achim Stahl[3], Luca Stanco[17], Korbinian Stangler[54], Konstantin Stankevich[49], Hans Steiger[54,22], Jochen Steinmann[3], Malte Stender[20], Tobias Sterr[21], David Stipp[22], Matthias Raphael Stock[54], Virginia Strati[60], Mikhail Strizh[49,50], Alexander Studenikin[49], Katharina von Sturm[25], Aoqi Su[57], Jun Su[8], Yuning Su[8], Gongxing Sun[4], Guangbao Sun[27], Hansheng Sun[4], Lijun Sun[4], Liting Sun[4], Mingxia Sun[4], Shifeng Sun[43], Xilei Sun[4], Yongzhao Sun[4], Yunhua Sun[4], Yuning Sun[8], Zhanxue Sun[84], Zhengyang Sun[76], Narumon Suwonjandee[12], Troy Swift[3], Michal Szelezniak[2], Dušan Štefánik[15], Fedor Šimkovic[15], Ondřej Šrámek[55], Dmitriy Taichenachev[10], Christophe De La Taille[24], Akira Takenaka[8], Hongnan Tan[4], Xiaohan Tan[39], Haozhong Tang[4], Jian Tang[8], Jingzhe Tang[37], Qiang Tang[8], Quan Tang[75], Xiao Tang[4], Jihua Tao[84], Eric Theisen[22], Minh Thuan Nguyen Thi[34], Renju Tian[4], Yuxin Tian[76], Alexander Tietzsch[21], Igor Tkachev[50], Tomas Tmej[55], Marco Danilo Claudio Torri[11], Francesco Tortorici[7], Konstantin Treskov[10], Andrea Triossi[25], Giancarlo Troni[1], Wladyslaw Trzaska[6], Andrei Tsaregorodtsev[26], Alexandros Tsagkarakis[3], Yu-Chen Tung[69], Cristina Tuve[7], Nikita Ushakov[50], Guillaume Vanroyen[18], Nikolaos Vassilopoulos[4], Carlo Venettacci[19], Giuseppe Verde[7], Maxim Vialkov[49], Benoit Viaud[18], Cornelius Moritz Vollbrecht[36,3], Vit Vorobel[55], Dmitriy Voronin[50], Lucia Votano[64], Stefan van Waasen[65], Stefan Wagner[80], Pablo Walker[30], Jiawei Wan[28], Andong Wang[84], Caishen Wang[38], Chung-Hsiang Wang[35], Cui Wang[71], Derun Wang[4], En Wang[57], Guoli Wang[59], Hanwen Wang[4], Hongxin Wang[28], Huanling Wang[4], Jiabin Wang[39], Jian Wang[4], Jun Wang[8], Ke Wang[46], Kunyu Wang[4], Lan Wang[4], Li Wang[57,4], Lu Wang[4], Meifen Wang[4], Meng Wang[39], Meng Wang[75], Mingyuan Wang[4], Qianchuan Wang[27], Ruiguang Wang[4], Sibo Wang[4], Siguang Wang[79], Tianhong Wang[59], Tong Wang[4], Wei Wang[8], Wei Wang[28], Wenshuai Wang[4], Wenwen Wang[28], Wenyuan Wang[39], Xi Wang[73], Xiangyue Wang[8], Xuesen Wang[8], Yangfu Wang[4], Yaoguang Wang[39], Yi Wang[40], Yi Wang[58], Yi Wang[4], Yifang Wang[4], Yuanqing Wang[40], Yuman Wang[28], Yuyi Wang[40], Zhe Wang[40],

Zheng Wang[4], Zhigang Wang[4], Zhimin Wang[4], Zongyi Wang[40], Apimook Watcharangkool[82], Junya Wei[39], Jushang Wei[39], Lianghong Wei[4], Wei Wei[4], Wei Wei[39], Wenlu Wei[4], Yadong Wei[38], Yuehuan Wei[8], Zhengbao Wei[37], Marcel Weifels[3], Kaile Wen[4], Liangjian Wen[4], Yijie Wen[4], Jun Weng[40], Christopher Wiebusch[3], Rosmarie Wirth[36,22], Steven Chan-Fai Wong[8], Bjoern Wonsak[20], Baona Wu[28], Bi Wu[8], Chengxin Wu[8], Chia-Hao Wu[34], Chin-Wei Wu[34], Diru Wu[4], Fangliang Wu[28], Jianhua Wu[4], Qun Wu[39], Shuai Wu[4], Wenjie Wu[42], Yinhui Wu[4], Yiyang Wu[40], Zhaoxiang Wu[4], Zhi Wu[4], Zhongyi Wu[47], Michael Wurm[22], Jacques Wurtz[2], Christian Wysotzki[3], Yufei Xi[61], Jingkai Xia[4], Shishen Xian[76], Ziqian Xiang[44], Fei Xiao[4], Pengfei Xiao[4], Tianying Xiao[37], Xiang Xiao[8], Wan Xie[4], Wei-Jun Xie[34], Xiaochuan Xie[37], Yijun Xie[4], Yuguang Xie[4], Zhangquan Xie[4], Zhao Xin[4], Zhizhong Xing[4], Benda Xu[40], Cheng Xu[75], Chuang Xu[40], Donglian Xu[76,44], Fanrong Xu[66], Hangkun Xu[4], Jiayang Xu[4], Jie Xu[62], Jilei Xu[4], Jinghuan Xu[37], Lingyu Xu[4], Meihang Xu[4], Shiwen Xu[4], Xunjie Xu[4], Ya Xu[83], Yin Xu[71], Yu Xu[63,3], Dongyang Xue[40], Jingqin Xue[4], Baojun Yan[4], Liangping Yan[4], Qiyu Yan[41,33], Taylor Yan[56], Tian Yan[4], Wenqi Yan[4], Xiongbo Yan[4], Yupeng Yan[56], Anbo Yang[4], Caihong Yang[4], Changgen Yang[4], Chengfeng Yang[8], Dikun Yang[46], Dingyong Yang[4], Fengfan Yang[4], Haibo Yang[28], Huan Yang[4], Jie Yang[57], Jize Yang[8], Kaiwei Yang[4], Lei Yang[38], Mengting Yang[39], Pengfei Yang[8], Xiaoyu Yang[4], Xuhui Yang[4], Yi Yang[4], Yichen Yang[4], Yifan Yang[53], Yixiang Yang[4], Yujiao Yang[71], Yuzhen Yang[28], Zekun Yang[39,9], Haifeng Yao[4], Li Yao[4], Jiaxuan Ye[4], Mei Ye[4], Xingchen Ye[27], Ziping Ye[76], Ugur Yegin[65], Frédéric Yermia[18], Peihuai Yi[4], Rattikorn Yimnirun[56], Jilong Yin[4], Na Yin[39], Weiqing Yin[4], Xiangwei Yin[4], Xiaohao Yin[8], Sivaram Yogathasan[3], Zhengyun You[8], Boxiang Yu[4], Chiye Yu[38], Chunxu Yu[71], Guangyou Yu[28], Guojun Yu[28], Hongzhao Yu[4,8], Miao Yu[27], Peidong Yu[4], Simi Yu[58], Xianghui Yu[71], Yang Yu[4], Zeyuan Yu[4], Zezhong Yu[4], Cenxi Yuan[8], Chengzhuo Yuan[4], Zhaoyang Yuan[4,8], Zhenxiong Yuan[40], Ziyi Yuan[27], Baobiao Yue[8], Noman Zafar[5], André Zambanini[65], Jilberto Zamora[81], Matteo Zanetti[16], Vitalii Zavadskyi[10], Fanrui Zeng[39], Pan Zeng[40], Shan Zeng[4], Tingxuan Zeng[4], Yuda Zeng[8], Yujie Zeng[8], Liang Zhan[4], Aiqiang Zhang[40], Bin Zhang[57], Binting Zhang[4], Chengcai Zhang[4], Enze Zhang[4], Feiyang Zhang[44], Guoqing Zhang[4], Haiqiong Zhang[4], Han Zhang[4], Hangchang Zhang[4], Haosen Zhang[4], Honghao Zhang[8], Hongmei Zhang[4], Jialiang Zhang[28], Jiawen Zhang[4], Jie Zhang[4], Jin Zhang[37], Jingbo Zhang[59], Jinnan Zhang[4], Junwei Zhang[37], Kun Zhang[4], Lei Zhang[28], Mingxuan Zhang[4], Mohan Zhang[4], Peng Zhang[4], Ping Zhang[44], Qingmin Zhang[67], Rongping Zhang[4], Rui Zhang[28], Shaoping Zhang[4], Shiqi Zhang[8], Shu Zhang[8], Shuihan Zhang[4], Siyuan Zhang[37], Tao Zhang[44], Xiaofeng Zhang[4], Xiaomei Zhang[4], Xin Zhang[4], Xu Zhang[4], Xuan Zhang[4], Xuantong Zhang[4], Xuesong Zhang[8], Xueyao Zhang[39], Yan Zhang[4], Yibing Zhang[4,45], Yinhong Zhang[4], Yiyu Zhang[4], Yizhou Zhang[4], Yongjie Zhang[4], Yongpeng Zhang[4], Yu Zhang[4], Yuanyuan Zhang[76], Yue Zhang[39], Yueyuan Zhang[4], Yumei Zhang[8], Yuning Zhang[41], Zhenyu Zhang[27], Zhicheng Zhang[39], Zhijian Zhang[38], Zhixuan Zhang[44], Baoqi Zhao[4], Fengyi Zhao[42], Jie Zhao[4], Liang Zhao[83], Mei Zhao[4], Rong Zhao[8], Runze Zhao[4,45], Shujun Zhao[57], Tianchi Zhao[4], Tianhao Zhao[4], Yubin Zhao[4], Dongqin Zheng[66], Hua Zheng[38], Xiangyu Zheng[71], Yangheng Zheng[41], Weili Zhong[4], Weirong Zhong[66], Albert Zhou[4], Guorong Zhou[58], Li Zhou[4], Lishui Zhou[46], Min Zhou[4], Shun Zhou[4], Tong Zhou[4], Xiang Zhou[27], Xing Zhou[4], Yan Zhou[40], Haiwen Zhu[27], Jiang Zhu[8], Jingsen Zhu[8], Jingyu Zhu[42], Kangfu Zhu[67], Kejun Zhu[4], Zhihang Zhu[4], Ivan Zhutikov[10], Bo Zhuang[4], Honglin Zhuang[4], Liang Zong[40], Jiaheng Zou[4], Sebastian Zwickel[54] & Jan Züfle[21]

[1]Pontificia Universidad Católica de Chile, Santiago, Chile. [2]IPHC, Université de Strasbourg, CNRS/IN2P3, Strasbourg, France. [3]III. Physikalisches Institut B, RWTH Aachen University, Aachen, Germany. [4]Institute of High Energy Physics, Beijing, China. [5]Pakistan Institute of Nuclear Science and Technology, Islamabad, Pakistan. [6]Department of Physics, University of Jyvaskyla, Jyvaskyla, Finland. [7]INFN Catania and Dipartimento di Fisica e Astronomia dell Università di Catania, Catania, Italy. [8]Sun Yat-sen University, Guangzhou, China. [9]The University of Liverpool, Department of Physics, Oliver Lodge Laboratory, Liverpool, UK. [10]Joint Institute for Nuclear Research, Dubna, Russia. [11]INFN Sezione di Milano and Dipartimento di Fisica dell Università di Milano, Milano, Italy. [12]High Energy Physics Research Unit, Faculty of Science, Chulalongkorn University, Bangkok, Thailand. [13]IJCLab, Université Paris-Saclay, CNRS/IN2P3, Orsay, France. [14]LLR, École Polytechnique, CNRS/IN2P3, Palaiseau, France. [15]Comenius University Bratislava, Faculty of Mathematics, Physics and Informatics, Bratislava, Slovakia. [16]INFN Milano Bicocca and University of Milano Bicocca, Milano, Italy. [17]INFN Sezione di Padova, Padova, Italy. [18]SUBATECH, Nantes Université, IMT Atlantique, CNRS/IN2P3, Nantes, France. [19]Dipartimento di Matematica e Fisica, Università Roma Tre and INFN Sezione Roma Tre, Roma, Italy. [20]Institute of Experimental Physics, University of Hamburg, Hamburg, Germany. [21]Eberhard Karls Universität Tübingen, Physikalisches Institut, Tübingen, Germany. [22]Institute of Physics and EC PRISMA+, Johannes Gutenberg Universität Mainz, Mainz, Germany. [23]Department of Physics, National Taiwan University, Taipei, https://www.phys.ntu.edu.tw/enphysics/Default.html. [24]Univ. Bordeaux, CNRS, LP2I, UMR 5797, Gradignan, France. [25]Dipartimento di Fisica e Astronomia dell'Università di Padova and INFN Sezione di Padova, Padova, Italy. [26]Aix Marseille Univ, CNRS/IN2P3, CPPM, Marseille, France. [27]School of Physics and Technology, Wuhan University, Wuhan, China. [28]Nanjing University, Nanjing, China. [29]INFN Milano Bicocca and Politecnico of Milano, Milano, Italy. [30]Millennium Institute for SubAtomic Physics at the High-energy Frontier (SAPHIR), ANID, Santiago, Chile. [31]China Nuclear Power Technology Research Institute, Shenzhen, China. [32]New Cornerstone Science Laboratory, Institute of High Energy Physics, Beijing, China. [33]University of Warwick, Coventry, United Kingdom. [34]Institute of Physics, National Yang Ming Chiao Tung University, Hsinchu, https://phys.nycu.edu.tw/en/. [35]National United University, Miao-Li, https://www.nuu.edu.tw/index.php?Lang=en. [36]GSI Helmholtzzentrum für Schwerionenforschung, Darmstadt, Germany. [37]Guangxi University, Nanning, China. [38]Dongguan University of Technology, Dongguan, China. [39]Shandong University, Jinan, and Key Laboratory of Particle Physics and Particle Irradiation of Ministry of Education, Shandong University, Qingdao, China. [40]Tsinghua University, Beijing, China. [41]University of Chinese Academy of Sciences, Beijing, China. [42]Institute of Modern Physics, Chinese Academy of Sciences, Lanzhou, China. [43]North China Electric Power University, Beijing, China. [44]School of Physics and Astronomy, Shanghai Jiao Tong University, Shanghai, China. [45]Kaiping Neutrino Research Center, Guangdong, China. [46]Department of Earth and Space Sciences, Southern University of Science and Technology, Shenzhen, China. [47]Department of Physics and Astronomy, University of California, Irvine, CA, USA. [48]Beijing Institute of Spacecraft Environment Engineering, Beijing, China. [49]Lomonosov Moscow State University, Moscow, Russia. [50]Institute for Nuclear Research of the Russian Academy of Sciences, Moscow, Russia. [51]Universidade Estadual de Londrina, Londrina, Brazil. [52]INFN Sezione di Perugia and Dipartimento di Chimica, Biologia e Biotecnologie dell'Università di Perugia, Perugia, Italy. [53]Université Libre de Bruxelles, Brussels, Belgium. [54]Technische Universität München, München, Germany. [55]Charles University, Faculty of Mathematics and Physics, Prague, Czech Republic. [56]Suranaree University of Technology, Nakhon Ratchasima, Thailand. [57]School of Physics, Zhengzhou University, Zhengzhou, China. [58]Wuyi University, Jiangmen, China. [59]Harbin Institute of Technology, Harbin, China. [60]Department of Physics and Earth Science, University of Ferrara and INFN Sezione di Ferrara, Ferrara, Italy. [61]Institute of Hydrogeology and Environmental Geology, Chinese Academy of Geological Sciences, Shijiazhuang, China. [62]China University of Geosciences, Beijing, China. [63]Forschungszentrum Jülich GmbH, Nuclear Physics Institute IKP-2, Jülich, Germany. [64]Laboratori Nazionali di Frascati dell'INFN, Roma, Italy. [65]Forschungszentrum Jülich GmbH, Central Institute of Engineering, Electronics and Analytics - Electronic Systems (ZEA-2), Jülich, Germany. [66]Jinan University, Guangzhou, China. [67]Xi'an Jiaotong University, Xi'an, China. [68]Department of Electro-Optical Engineering, National Taipei University of Technology, Taipei, https://eo.ntut.edu.tw/index.php?Lang=en. [69]Department of Physics, National Kaohsiung Normal University, Kaohsiung, https://phy.nknu.edu.tw/en_phy.htm. [70]Yerevan Physics Institute, Yerevan, Armenia. [71]Nankai University, Tianjin, China. [72]Chengdu University of Technology, Chengdu, China. [73]College of Electronic Science and Engineering, National University of Defense Technology, Changsha, China. [74]China Institute of Atomic Energy, Beijing, China. [75]University of South China, Hengyang, China. [76]Tsung-Dao Lee Institute, Shanghai Jiao Tong University, Shanghai, China. [77]University of Science and Technology of China, Hefei, China. [78]Xiamen University, Xiamen, China. [79]School of Physics, Peking University, Beijing, China. [80]Pontificia Universidade Catolica do Rio de Janeiro, Rio de Janeiro, Brazil. [81]Universidad Andres Bello, Fernandez Concha, Chile. [82]National Astronomical Research Institute of Thailand, Chiang Mai, Thailand. [83]Institute of Geology and Geophysics, Chinese Academy of Sciences, Beijing, China. [84]East China University of Technology, Nanchang, China. [85]Deceased: Jingzhi Bai, Tobias Drohmann, Gianfranco Giordano, Zinovy Krumshteyn, Weiguo Li, Andrey Sadovsky.

Methods

Oscillation of reactor $\bar{\nu}_e$

In the three-neutrino oscillation framework, the flavour states ($\nu_e/\bar{\nu}_e$, $\nu_\mu/\bar{\nu}_\mu$, $\nu_\tau/\bar{\nu}_\tau$) are connected with the mass eigenstates ($\nu_1/\bar{\nu}_1$, $\nu_2/\bar{\nu}_3$, $\nu_3/\bar{\nu}_3$) by the leptonic mixing matrix[7–9] parametrized by three mixing angles θ_{12}, θ_{23}, θ_{13} and one complex phase δ (ref. 3). The oscillation frequencies are determined by the three mass-squared differences $\Delta m^2_{ij} \equiv m_i^2 - m_j^2$, $(i, j = 1, 2, 3, i > j)$, where m_i is the ν_i mass. Typical approximate values for the mixing angles are $\theta_{12} \approx 33°$ (refs. 13,52), $\theta_{23} \approx 45°$ (refs. 56–63) and $\theta_{13} \approx 8.5°$ (refs. 41,64,65). The solar mass-squared splitting is $\Delta m^2_{21} \simeq 7.4 \times 10^{-5}$ eV^2 (refs. 13,52,55), whereas the atmospheric splitting is about two orders of magnitude larger, $|\Delta m^2_{31}| \simeq 2.5 \times 10^{-3}$ eV^2 (refs. 41,56–59,64,66–68). Although ordering of the first two mass states ($m_2 > m_1$) is known, the ordering of m_3—normal or inverted—remains undetermined.

When neutrinos propagate in matter, oscillation parameters acquire the corrections from the effective matter potential[69,70], denoted by tilded quantities $\widetilde{\theta}_{ij}$ and $\Delta\widetilde{m}^2_{ij}$. For JUNO, matter effects are minor[50,71], and its main sensitivity to oscillation parameters $\sin^2\theta_{12}$, Δm^2_{21} and Δm^2_{31} and to neutrino mass ordering arises from vacuum oscillations.

The IBD interaction used to detect reactor neutrinos is sensitive only to the electron flavour. Consequently, the relevant oscillation observable is the electron antineutrino survival probability $\mathcal{P}_{ee} \equiv \mathcal{P}(\bar{\nu}_e \to \bar{\nu}_e)$ that can be expressed as

$$\begin{aligned}\mathcal{P}_{ee} = 1 - &\sin^2 2\widetilde{\theta}_{12}\, \tilde{c}_{13}^4 \sin^2\widetilde{\Delta}_{21} \\ &- \sin^2 2\widetilde{\theta}_{13}(\tilde{c}_{12}^2 \sin^2\widetilde{\Delta}_{31} + \tilde{s}_{12}^2 \sin^2\widetilde{\Delta}_{32}).\end{aligned} \tag{1}$$

where $\tilde{c}_{ij} \equiv \cos\widetilde{\theta}_{ij}$, $\tilde{s}_{ij} \equiv \sin\widetilde{\theta}_{ij}$ and $\widetilde{\Delta}_{ij} = \Delta\widetilde{m}^2_{ij} L / 4E_{\bar{\nu}_e}$, with $E_{\bar{\nu}_e}$ being the antineutrino energy and L the baseline from reactor cores to the detector. The first 'solar term' represents the slow oscillation associated with Δm^2_{21}, whereas the second 'atmospheric term' characterizes the fast oscillation, as shown by the red and blue curves in Extended Data Fig. 1, respectively.

For a typical antineutrino energy of 4 MeV, the solar oscillation length is 60 km, whereas the atmospheric oscillation length is about 2 km. The 52.5 km baseline of JUNO is near the first solar oscillation maximum, allowing it to probe the interference with atmospheric oscillations and thus determine the neutrino mass ordering. Simultaneously, $\mathcal{P}_{ee}$ is near its minimum, forcing JUNO to be an exceptionally large detector to gather sufficient statistics for its physics goals.

JUNO detector setup

The main JUNO detector components, CD, WP and top tracker, are shown in Fig. 1.

The CD[24] represents the core part of the experiment. It contains 20 ktonne of LS enclosed in a 35.4-m diameter acrylic spherical (AV), constructed from highly transparent acrylic panels and held in place by a supporting stainless steel structure (SSS). The optimization of the LS mixture, reported in refs. 72,73, was performed using a Daya Bay detector and a comprehensive optical model, with the results extrapolated to the JUNO scale. The JUNO LS consists of linear alkyl benzene (LAB) as solvent, 2.5 g l^{-1} PPO as primary fluor, 3 mg l^{-1} bis-MSB as wavelength shifter, and 42.7 mg l^{-1} BHT as antioxidant to prevent long-term optical degradation. The 17,596 20-inch 'large' photomultiplier tubes (LPMTs) provide the primary photon detection, achieving approximately 75% geometrical coverage. This includes 4,939 dynode PMTs and 12,657 micro-channel plate (MCP) PMTs mounted on the support structure. An additional 25,587 3-inch 'small' PMTs (SPMTs) are installed among the LPMTs (3% geometrical coverage) to extend the dynamic range and enhance the precision of calibration.

The CD is installed inside a cylindrical WP, 43.5 m in diameter and 44.0 m in height, that is filled with 41 ktonne of high-purity water (^{238}U/^{232}Th < 10^{-15} g g^{-1}, ^{222}Rn < 10 mBq m^{-3}, ^{226}Ra < 50 μBq m^{-3}) characterized by a light attenuation length of >60 m. The water pool shields the central detector against external radiation and acts as a water Cherenkov detector using 35 ktonne of water for the residual cosmic-ray muon flux. The remaining 6 ktonne of water are used in the CD region between the SSS and the AV as a shield against external background. Cherenkov photons produced by cosmic muons are detected by 2,752 MCP PMTs and additional 600 eight-inch R5912 PMTs. The water Cherenkov detector is optically separated from the central detector by Tyvek reflective foils. The muon-tagging efficiency is very close to 100%, with a very small geometrical inefficiency (<0.02%) because of the top chimney, which connects the top of the CD to the calibration house above it.

The cosmic muon veto system is complemented by an external top track system, consisting of three layers of plastic scintillator refurbished from the OPERA experiment[74], covering approximately 60% of the top surface above the WP. Its primary purpose is to provide a sample of muons, reconstructed with an angular precision of 0.20° (ref. 75), which can be used to benchmark the track reconstruction of the WP and CD.

The CD calibration strategy[37] is designed to use four source-deployment subsystems—the automatic calibration unit (ACU), the cable loop system (CLS), the guide tube (GT) and a remote-operated vehicle (ROV)—which together allow precise placement of radioactive and optical sources along the central axis of the detector, within radial planes, at the detector boundary, and at arbitrary three-dimensional positions, respectively. In the water Cherenkov detector, LED flashers installed along the WP wall and on the bottom are used to perform the PMT timing calibration.

Detector filling and commissioning

The JUNO detector was filled from December 2024 to August 2025 with the support of dedicated auxiliary facilities. The CD and WP were first filled simultaneously with water from the high-purity water plants, then the water in the CD was gradually replaced with high-purity LS under nitrogen protection. The LS purification process included alumina filtering, vacuum distillation, mixing with PPO, bis-MSB and BHT to form the master solution, water washing and underground water extraction and nitrogen stripping. The filling, overflow and circulation system managed the liquid levels, ensured structural safety, and allowed online recirculation if needed. OSIRIS, a 20-tonne scintillator detector[76], monitored LS samples for radioactivity during production.

The detector commissioning was carried out simultaneously with the water filling and LS exchange. JUNO online LPMT waveforms and event reconstructions enabled real-time ^{222}Rn monitoring, keeping contamination below 1 mBq m^{-3}. The LS reached an attenuation length of 20.6 m at 430 nm, and radiopurity measurements in the FV showed ^{238}U and ^{232}Th levels of $(7.5 \pm 0.9) \times 10^{-17}$ g g^{-1} and $(8.2 \pm 0.7) \times 10^{-17}$ g g^{-1}, respectively, exceeding the design requirements of JUNO. The background from unsupported ^{210}Po, averaged over the analysed period, was $(4.3 \pm 0.3) \times 10^4$ cpd ktonne^{-1}. This performance results from stringent material selection, advanced purification and meticulous assembly protocols—including continuous leak-checking, surface treatments and clean-room installation[77].

JUNO uses a full waveform readout of all LPMTs digitized by underwater global control units and processed through a multiplicity-based global trigger. Each LPMT generates a 'hit' when the signal exceeds five times the noise of the channel. A global trigger is issued when 350 PMTs fire within a 304 ns window, resulting in an overall trigger rate of about 500 Hz. The data acquisition gate has a duration of 1,008 ns. Conversely, SPMTs have a self-trigger threshold of 0.33 p.e. The online event classification system performs real-time waveform and event reconstruction to select relevant physics events, for which full waveforms are stored, reducing the data rate to about 90 MB s^{-1}. No triggered events are discarded.

For more information on the JUNO detector, see ref. 4. We also refer readers to ref. 36 for a comprehensive report on the initial performance and operational details of the JUNO detector, focusing on the in situ calibration of the 20-inch PMTs and readout electronics, energy response characterization (including light yield, energy scale, non-uniformity, non-linearity and resolution), transparency and radiopurity of the liquid scintillator, muon identification efficiency and overall system stability. That work also details three independent event reconstruction algorithms used in the oscillation analyses. The following sections elaborate on the methodological specifics of the reactor neutrino oscillation analysis.

Calibration strategy

At the beginning of data taking, from 23–26 August, a calibration campaign was carried out to calibrate the PMTs, establish the energy scale and characterize the detector response. The ACU deployed five γ sources—^{68}Ge (2 × 511 keV from e^+ annihilation), ^{137}Cs (661.7 keV), ^{54}Mn (834.8 keV), ^{40}K (1,460.8 keV) and ^{60}Co (1,173.2 keV and 1,332.5 keV)—together with an AmC neutron source and an ultraviolet (UV) laser at the detector centre and at two off-centre positions (±14 m), with placement controlled to better than 1 cm. Additional AmC neutron-source calibration was performed: 7 points with the ACU and 39 off-axis points with the source attached to the CLS, enabling calibration along a vertical half-plane with a positioning precision of about 3 cm. The light yield was biweekly monitored with the AmC source deployed at the detector centre.

The LPMT calibration program monitors charge response, gain, timing and dark noise using weekly UV-laser runs and a 50 Hz periodic trigger. The charge spectra of the laser LPMTs were fit with models tailored separately for dynode PMTs and for MCP PMTs[36]. The average mean gain—6.5×10^6 for dynode PMTs and 7.2×10^6 for MCP PMTs—remained stable over time within 0.2%. The relative photon detection efficiency of each PMT was calibrated using isotropic light produced by the AmC source at the CD centre. The transit time spread (TTS) was calibrated with laser data from the full water phase. The average values were 7.5 ns for MCP PMTs and 1.9 ns for dynode PMTs.

PMT timing calibration uses pulsed laser light delivered to the detector, with a fast monitor PMT providing a precise t_0 reference. Residual time distributions—obtained from first-hit times corrected for photon time of flight—allow the extraction of the TTS and the determination of per-channel time offsets. After calibration, the PMTs achieve sub-nanosecond synchronization across the whole detector.

PMT dark noise was monitored using periodic triggers, yielding average dark rates of 20.6 kHz for dynode PMTs and 22.7 kHz for MCP PMTs. Channels with low occupancy (about 2–3%) or timing misalignment (<0.1%) were excluded from analysis.

Reconstruction

LPMT waveform reconstruction. The JUNO analysis chain starts from waveform reconstruction of LPMTs. The digitized waveforms are reconstructed to extract the pulse time (t) and charge (Q). The resulting (t, Q) pairs serve as inputs for the subsequent event reconstruction. A simple yet robust continuous over-threshold integral (COTI) algorithm was selected as the baseline for this data analysis. COTI identifies pulses by first calculating the waveform baseline and then scanning 8 ns windows for consecutive points above or below a threshold to determine the pulse start and end times, respectively. The pulse charge is obtained by numerically integrating the waveform between these times. The pulse time is determined by fitting a straight line to the rising edge of the pulse and finding where it intersects the baseline. The COTI threshold corresponds to approximately 0.25 p.e.

Point-like event reconstruction. Event reconstruction primarily consists of vertex determination, relying mostly on PMT timing, and energy reconstruction, heavily dependent on PMT charge. After correcting for photon time of flight and the event start time, residual hit-time distributions—usually based on the earliest hits—are constructed. The corresponding PDFs are primarily shaped by the scintillation time profile and the PMT TTS. The amount of charge seen by PMT depends on the event energy but also on its position within the LS volume. Several reconstruction algorithms were used for this analysis and all provided overall consistent results.

OMILREC[78], a combined time- and charge-likelihood method, was developed to simultaneously reconstruct the event vertex and energy. Its time likelihood calculation uses the aforementioned residual hit-time PDFs, derived from the ^{68}Ge source at detector centre and constructed separately for dynode and MCP PMTs. The charge likelihood is based on the expected PMT charge response, parameterized using the ^{68}Ge source at various positions and natural sources such as ^{214}Po. By integrating both charge and timing information, the method significantly improved vertex resolution by about 25–50% (ref. 36), particularly for events near the detector edge, with respect to using timing information only.

In an alternative approach, OMILREC reconstructs the energy relying on a vertex provided by the JVertex algorithm. The timing PDFs for JVertex are derived from AmC calibration data obtained with the ACU system and constructed using only dynode PMTs, which offer superior timing performance. Separate PDFs are produced according to the detected photon multiplicity, to account for cases in which multiple photons are registered by the same PMT within its time resolution. Similar to OMILREC, the vertex is determined by maximizing the likelihood function.

VTREP is an independent algorithm reconstructing both vertex and energy. The vertex is reconstructed by identifying the position at which the time-of-flight correction produces the sharpest PMT hit-time distribution, taking into account the detector geometry and light refraction at the acrylic boundary[79]. The particle energy is obtained by maximizing a likelihood function that incorporates the probabilities of both fired and unfired PMTs, based on the predicted light intensity at each PMT. The light intensity prediction and probability density functions were obtained from uniformly distributed ^{214}Po events from the ^{214}Bi–^{214}Po decay cascade and laser calibration samples, respectively[80].

Muon track reconstruction. A cluster-finding algorithm is applied to the PMT charge distribution of muon candidates to identify localized regions of high charge associated with muon entry and exit points. For events with two or more clusters, muon tracks are reconstructed as straight lines connecting the charge-weighted centres of the entry and exit clusters. The resulting angular distributions of reconstructed muons agree well with Monte Carlo predictions[36].

Detector response model

In this section, we discuss the relationship between the detector response and reconstructed variables and different particle types depositing energy in the detector volume. In an LS detector such as JUNO, this encompasses characterization of the effective light yield, non-linearity of the energy scale, energy resolution and the residual spatial non-uniformity across the large detector volume. These effects must be precisely modelled and calibrated to achieve accurate prediction of the energy spectra of the reactor neutrino signal as well as all backgrounds.

Effective light yield. The energy scale is anchored to the 2.223 MeV gamma peak originating from neutron capture on protons. The effective light yield of approximately 1,785 p.e. MeV^{-1} was calibrated using the neutron-capture peak from an AmC neutron source deployed at the detector centre[36]. It encompasses all detector effects, including the number of emitted photons, their propagation through the detector and the detection probability at the PMTs.

Energy scale non-linearity. The visible energy in the LS is not proportional to the deposited energy. Moreover, different particles

depositing the same energy produce different numbers of photons. These non-linearities arise from ionization quenching, dependent on the particle stopping power dE/dx, and from the Cherenkov photons. Instrumental non linearity may also arise during the charge reconstruction of PMT waveforms.

The non-linearity model is constrained using three calibration datasets: (1) reconstructed visible energy from eight γ sources with energies ranging from 0.511 MeV to 6.13 MeV (^{137}Cs, ^{54}Mn, ^{40}K, ^{68}Ge, nH, ^{60}Co, n^{12}C and ^{16}O*), deployed at the detector centre. The de-excitation gamma from neutron absorption on Fe (n^{56}Fe) in the source capsule was used for additional validation; and two kinds of continuous spectra from high-purity samples of cosmogenic isotopes reconstructed in the FV, namely (2) ^{12}B electron spectrum (Q = 13.37 MeV) and (3) ^{11}C positron spectrum (Q = 0.96 MeV), with visible energy increased by 2 × 511 keV annihilation gammas.

To accurately extract the reconstructed energy peak and its spread for each gamma source, comprehensive spectral fitting was performed, incorporating all relevant transitions contributing to the spectrum. Potential influence of backgrounds, such as those arising from ^{14}C pileup, was also evaluated and incorporated in the fit. Systematic uncertainties, including energy leakage due to source encapsulation (0.1%) and peak stability (<0.2%), were also quantified. The ^{12}B sample exhibited a purity exceeding 96%, with the expected ^{12}N component (about 2.5%) explicitly accounted for in the spectral modelling.

The non-linearity model uses the energy spectra of secondary electrons from Compton scattering of γs, obtained from Geant4 simulations and their stopping power, as obtained from the ESTAR[81] database. Ionization quenching is modelled using Birks's law[82] with the coefficient k_B being a free fit parameter. Cherenkov light contribution is modelled using either Geant4-based parametric functions or the Frank–Tamm formula[83], with the relative strength controlled by a free parameter k_C. An additional parameter A accounts for the absolute scintillation energy scale. The instrumental non-linearity was modelled using either a linear or exponential function, with both forms anchored at the nH capture peak. All model parameters are determined through χ^2 minimization to the combined calibration data, and the treatment of systematic uncertainties follows the strategy of ref. 39. Extended Data Fig. 2 shows the best-fit results to the mono-energetic peaks from gamma calibration sources and the continuous energy spectra from cosmogenic isotopes, as well as the predicted electron and positron non-linearities. In Extended Data Fig. 2a, the effective gamma energy is defined as the true gamma energy for a single gamma-ray. For calibration sources emitting multiple gammas (for example, from ^{68}Ge, ^{60}Co or n^{12}C capture), the effective gamma energy represents the branching-ratio-weighted average of the visible energy per gamma, after accounting for the best-fit scintillator non-linearity. An overall non-linearity uncertainty of ±0.6% is achieved for positrons.

Three analysis groups adopted slightly different approaches in constructing non-linearity models and use of calibration data. Comparisons show that including or excluding instrumental non-linearity for centrally located gamma calibration sources has minimal impact (<0.2%) on the positron non-linearity results; a similar conclusion holds when incorporating n^{56}Fe γ data. Non-linearity measurements at off-centre positions (z = ±14 m) show no significant deviation from the centre, with variations <0.4% included in the overall energy scale systematics. Consequently, the positron non-linearity curves from the three analyses agree within 0.5%.

Energy resolution. The energy resolution for positrons is crucial for the neutrino mass ordering analysis[5], but is less critical for determining the solar oscillation parameters presented here. Studies of the energy resolution achieved for γs at the detector centre[36] show slightly worse performance than predicted by Monte Carlo simulations[25]. Resolution for the ^{68}Ge source is approximately 3.4%.

Antineutrino event selection

The selection of reactor neutrino candidates is based on following criteria: (1) spatio-temporal prompt-delayed coincidence to maintain high signal efficiency; (2) an FV cut to suppress backgrounds caused by external radioactivity (accidental coincidences and fast neutrons from undetected muons); (3) dedicated muon veto strategy to reject cosmogenic backgrounds; (4) a multiplicity cut to further reject neutron-related background from undetected muons and instrumental backgrounds. Before these selections, the spontaneous light emission in PMT ('flashers') was suppressed by applying cuts on the standard deviations of the PMT hit multiplicity and timing distributions. The overall detection efficiency was determined through a detailed evaluation of individual selection criteria. Independent analyses using alternative reconstructions and selection criteria confirmed statistically consistent results.

Prompt-delayed coincidence cuts. Applied in the selection are as follows: a prompt energy $0.7 < E_p < 12.0$ MeV, a delayed energy $2.0 < E_d < 2.5$ MeV, a time interval 5 μs < Δt < 1 ms and a spatial separation Δd < 1.5 m between prompt and delayed signals.

Energy-selection efficiencies were validated with calibration data. The prompt-energy cut was fully efficient above threshold, as verified using a ^{68}Ge source. The delayed-energy window retained 99.99% of events from neutron captures on protons with 0.1% relative uncertainty due to energy resolution. The temporal-coincidence efficiency, determined from an exponential fit to the Δt distribution of IBD candidates, was 96.8% with a 0.02% relative uncertainty due to capture-time variation. The spatial-correlation cut preserved 98.3% of events with a relative uncertainty of 0.1%, derived from the reconstructed IBD Δr distribution. Both the temporal- and spatial-coincidence efficiencies are verified using AmC sources and Monte Carlo simulations.

Fiducial volume cut. Prompt positron candidates are required to have radius R < 16.5 m and $|z|$ < 15.5 m to strongly suppress accidental and cosmogenic neutron backgrounds and to minimize the impact of biases in the reconstruction algorithms. Alternative analyses used different vertex reconstruction algorithms and adopted slightly different criteria, such as applying a separate R < 17.2 m for the delayed signal, or limiting the polar region cut only around the z-axis ($|z|$ > 15.5 m and $\rho = \sqrt{x^2 + y^2}$ < 2 m). Across all reconstruction methods and FV definitions, the total efficiency variation remained below 1%. Extended Data Fig. 3 shows the radial distributions of prompt IBD candidates using three independent vertex reconstruction algorithms. As it can be seen, the distributions are uniform within the FV and the rate increase at larger radii is limited to the volume with R > 16.5 m.

The FV efficiency is obtained from the geometrical volume fraction accepted in the selection (80.6%), under the assumption of a uniform IBD distribution within the FV. We performed independent estimations using a ^{12}B sample and a high-energy (>3.5 MeV) IBD sample by calculating the fraction of these events reconstructed inside the FV relative to the total. For the high-energy IBD sample, this validation is consistent with a precision comparable to the assigned FV-related uncertainty. For the ^{12}B sample, the effective validation precision is limited by systematic effects associated with its non-uniform spatial distribution, which is correlated with parent muon tracks, and is therefore less constraining for the absolute FV efficiency. Overall, these results were consistent with the nominal method within the quoted uncertainty.

The spread among the different reconstruction algorithms near the fiducial boundary yields a 1.6% relative FV efficiency uncertainty. Possible energy dependence of this FV-related uncertainty is examined using high-statistics cosmogenic ^{12}B events, and no significant energy-dependent effect is observed within the assigned uncertainty. An independent estimate based on the measured about 10 cm vertex-reconstruction bias at the FV boundary, as determined from

ACU source deployments, yields a comparable approximately 1.8% relative uncertainty.

In the muon veto, events were rejected if the delayed signal occurred within 5 ms of a preceding muon, or if it was found within 4 m of an identified spallation neutron (SPN) and within 1.2 s after that neutron (namely, spallation-neutron veto). Muon candidates were identified as CD triggers with charge $Q > 3 \times 10^4$ p.e. or WP triggers with $Q > 700$ p.e. The detector-wide veto of 5 ms following muon events in the central detector or water Cherenkov detector results in a livetime efficiency of 95.55%, with negligible uncertainty.

Spallation neutrons were identified by their timing ($20\ \mu s < \Delta t_\mu < 2$ ms after a muon) and either their charge ($3{,}000 < Q < 3 \times 10^4$ p.e.) or, equivalently, their reconstructed energy ($1.5 < E < 20$ MeV). We also tested an additional selection based on the spread of the hit-time distribution to suppress afterpulse contamination and obtained consistent results. The spallation-neutron veto acts only in localized regions, and the veto efficiency for these localized events was determined by segmenting the detector into 10-cm cubes and integrating their livetimes, yielding 98.0% with negligible uncertainty. The spallation-neutron veto removes >90% of ^{9}Li/^{8}He events. An independent analysis using a track-based veto applied around reconstructed muon trajectories had a further 25% suppression of the residual ^{9}Li/^{8}He, with a 0.6% reduction in signal efficiency.

Multiplicity cut. It removed events with additional energy deposits above 0.7 MeV (within the FV) or in the [2.0, 2.5] MeV range (outside it) within a $[t_d - 2\ \text{ms}, t_d + 1\ \text{ms}]$ window. The multiplicity-cut efficiency evaluated based on the above-mentioned method was 97.4%. The livetime approach provides a direct, model-independent measurement, whereas an analytic estimate based on the singles rate serves as a cross-check and agrees with the livetime method. Two other analyses using slightly different energy thresholds and fiducial requirements showed about 1% efficiency variation.

The characteristics of reactor neutrino candidates are shown in Extended Data Fig. 4. The two-dimensional prompt and delayed energy plot shows a clear signal concentration within the selection window (red box), with correlated backgrounds from ^{214}Bi–^{214}Po decay dominating at lower energies. Furthermore, the prompt-delayed signal pairs exhibited strong agreement with predicted temporal and spatial correlations.

Backgrounds

The following backgrounds remain for IBDs: correlated backgrounds from the β–n cascade of ^{9}Li/^{8}He decays, geoneutrinos, a rare branch in β–α cascade of ^{214}Bi–^{214}Po decays, remote reactors, fast neutrons, ^{13}C(α, n)^{16}O, and atmospheric neutrino neutral–current (NC) interactions, and uncorrelated backgrounds from accidental coincidence. The estimated background rates are shown in Table 1. Below, we provide additional details for some backgrounds.

Cosmogenic ^{9}Li/^{8}He background. The dominant background originates from cosmogenic β–n emitters ^{9}Li and ^{8}He. Their rates were extracted from the time distribution between antineutrino candidates and their most recent preceding muons, both before and after veto application. These preceding muons were required to be tagged by both the CD and WP detectors. At high muon rates, however, this method becomes uncertain because of the similar timescales of isotope decays and genuine antineutrino signals. We, therefore, performed a combined fit across four muon energy intervals (all with visible energy above 0.6 GeV and similar muon rates), explicitly accounting for correlations arising from ^{9}Li/^{8}He events produced in one interval and appearing as antineutrino candidates in others. The ^{9}Li/^{8}He ratio was constrained by the measurement from Daya Bay[40].

Rate uncertainties were derived from the covariance matrix of the interval counts and validated using a bootstrap method that accounts for correlations within the dataset. A systematic uncertainty arises as the muon selection may miss the true parent of ^{9}Li/^{8}He, as assessed by varying the joint CD–WP muon-tagging requirements that changed the fitted rate by 6%. Varying the ^{8}He-to-^{9}Li ratio by up to 10% shifts the central value by only 2%. Moreover, the difference between the residual ^{9}Li/^{8}He rates after applying the same selection criteria in data and Monte Carlo is 11%. Combining these with the statistical uncertainty, an overall 35% uncertainty is assigned to the ^{9}Li/^{8}He background rate.

The ^{9}Li/^{8}He production is typically accompanied by neutron emission, as indicated by both simulations (Geant4[84] and FLUKA[85,86]) and previous Daya Bay results[17]. The spallation-neutron veto mentioned in context rejected more than about 90% of ^{9}Li/^{8}He background, exceeding 97% for muons with visible energy above 10 GeV, as shown in Extended Data Fig. 5. One analysis further applied a cylinder veto within 1 m and 0.5 s along muon tracks of single muons without spallation-neutron tags, providing a small additional reduction.

To improve the time-since-last-muon fit, an alternative method selected only muons accompanied by spallation neutrons, which are more likely to produce ^{9}Li and ^{8}He. This selection reduced the muon rate and alleviated degeneracies in the fit. Using a ^{9}Li/^{8}He-enriched sample from IBD candidates within certain distances of muon tracks, the neutron accompaniment efficiency was measured as (90 ± 2)% by comparing yields with and without the SPN requirement. Both methods gave consistent production rates, and the residual ^{9}Li/^{8}He background was estimated by subtracting the expected IBD signal.

A high-purity ^{9}Li/^{8}He sample, tagged by associated spallation neutrons, enabled spectral comparison with a spectrum calculated from nuclear databases and an empirical model first developed for Daya Bay[87], constraining spectral shape uncertainty to 20%. Furthermore, muons passing through the top tracker system[75] provided a calibrated sample to validate the near-exponential lateral distance distribution between β–n emitters and parent muons.

Geoneutrino background. Geoneutrinos, electron antineutrinos produced in the decay chains of ^{232}Th and ^{238}U within the crust and mantle of Earth, constitute an intrinsic background in reactor neutrino analyses. According to various geological models of the crust and mantle[88–91], the predicted geoneutrino flux would lead to (1.1–2.4) IBD events per day in the LS under the assumption of 100% detection efficiency[28]. Accordingly, we adopt a nominal rate of 1.75 events per day, with a 40% rate uncertainty included to cover the range of model predictions. To account for spectral-related systematic uncertainties, we assign a 5% bin-to-bin shape uncertainty, which accommodates variations among two spectral models[42,43], as well as compositional differences and oscillation effects. Moreover, a 10% uncertainty is applied to the nominal ^{232}Th/^{238}U signal ratio of 0.29, reflecting possible variations in this parameter.

^{214}Bi–^{214}Po background. During the LS filling phase, a ^{214}Bi–^{214}Po background was identified. Although the ^{214}Po α-particle energy is strongly quenched and typically falls below the delayed-energy threshold, a subset of higher energy events above the ^{214}Po peak has been observed. These events can originate either from the excited states of ^{214}Po observed by Borexino[92] or from the α-proton elastic scattering, reported by SNO+[55]. In both cases, the alpha is accompanied by a particle (γ or proton, respectively) with smaller quenching and thus higher visible energy and can eventually extend into the IBD delayed-energy window. This effect was quantified using data from the initial high-radon phase of JUNO filling. Scaling the measured tail fraction by the ^{214}Bi–^{214}Po rate during the physics dataset yields a background contribution of (0.18 ± 0.10) per day. The ^{214}Bi decay spectrum was measured in situ with high statistics by means of the ^{214}Bi–^{214}Po cascade; the associated shape uncertainty is conservatively estimated at 5% bin-to-bin uncorrelated.

Accidental background was measured using an off-time window method, applying identical selection criteria to those used in the standard IBD analysis, except for the prompt-delayed coincidence timing.

Within the FV, the rate was determined to be $(4.9 \pm 0.3) \times 10^{-2}$ day^{-1}. The uncertainty in the rate and shape of this background was estimated from the statistics of off-window events.

Atmospheric neutrino neutral–current interactions on carbon nuclei produce neutrons, generating correlated IBD-like backgrounds[93]. The rate was estimated using state-of-the-art neutrino interaction models[94,95] with the Honda atmospheric flux calculation[96]. Model dependence was evaluated by comparing GENIE 3.0.6 (ref. 94) and NuWro 19.02 (ref. 95) generators, including initial nuclear models and final-state interaction variations, with nuclear de-excitation simulated by TALYS[97]. The model-averaged prediction is 0.12 day^{-1} (pre-selection), with a conservative 50% uncertainty covering interaction modelling, de-excitation and flux systematics. A 50% bin-to-bin spectral shape uncertainty was determined from deviations among the selected models.

Neutron backgrounds. Cosmic-ray muons untagged by the WP or passing through the surrounding rock produce energetic neutrons that create correlated backgrounds through two mechanisms: fast neutrons mimic IBD signals by proton recoil followed by neutron capture, whereas double neutrons arise from sequential capture of two neutrons. The muon veto (>99.9% efficient) and the stringent FV cut reduced these to negligible levels (Extended Data Fig. 3). Simulations predict residual rates of 0.02 day^{-1} (fast neutrons) and 0.05 day^{-1} (double neutrons), concentrated near the LS edge and confirmed with corner-clipping muon data. The fast-neutron spectrum was obtained from muon-tagged events, whereas the double-neutron prompt spectrum used the IBD delayed-capture shape. Both backgrounds were assigned a conservative 100% rate uncertainty, supported by the absence of excess events in the >12 MeV IBD sideband (fast neutrons) and near the edge of the FV in Extended Data Fig. 3 (double neutrons). The fast-neutron spectrum uncertainty was evaluated by comparing constant and first-order (linear) fits; the difference was taken as a conservative estimate of 60%. The double-neutron spectrum is more sensitive to energy-scale uncertainties: a 50% shape uncertainty was conservatively assigned by applying a uniform ±1% shift to the reconstructed energy of the entire spectrum and comparing the resulting distribution with the nominal one.

^{13}C(α, n)^{16}O background. Alpha particles emitted by radioactive contaminants of the LS can be captured on ^{13}C nuclei (1.1% isotopic abundance), resulting in the emission of MeV-scale neutrons. A prompt signal can arise before the delayed neutron capture from neutron elastic scattering on protons, its inelastic interactions with ^{12}C, or from de-excitation γs emitted by ^{16}O nuclei produced in excited states, yielding a signature that mimics that of an IBD signal. This background has been recently revised using the open-source SaG4n software[98] as well as Geant4-based simulations. The detector response to reaction products was simulated with JUNO Monte Carlo. Considering the achieved radiopurity of the LS, this background was found to be very small (0.04 day^{-1}). About 95% of the backgrounds originate from α decays of ^{210}Po that is out of secular equilibrium with the ^{238}U chain. Rate and shape uncertainties of 25% or 50% were assigned by different groups considering different approaches in tuning the Monte Carlo response, in particular to protons and αs.

Reactor flux prediction and uncertainties

The predicted number of IBD events in reconstructed-energy ith bin is

$$N_i = C \times \int_{E_i^{\mathrm{rec}}}^{E_{i+1}^{\mathrm{rec}}} \mathrm{d}E^{\mathrm{rec}} \int \mathrm{d}E_{\bar{\nu}_e} \int_{-1}^{1} \mathrm{d}\cos\theta \times \sum_r \frac{\mathcal{P}_{ee}(E_{\bar{\nu}_e}, L_r)}{4\pi L_r^2} S_r(E_{\bar{\nu}_e}) \times \frac{\mathrm{d}\sigma}{\mathrm{d}\cos\theta}(E_{\bar{\nu}_e}, \cos\theta) R(E^{\mathrm{rec}}|E_{\bar{\nu}_e}), \quad (2)$$

where E^{rec} is the reconstructed prompt energy, $E_{\bar{\nu}_e}$ the antineutrino energy and L_r is the baseline from reactor core r to JUNO. $\mathcal{P}_{ee}$ is the electron antineutrino survival probability, S_r the emitted spectrum of core r, θ the positron scattering angle, $\frac{\mathrm{d}\sigma}{\mathrm{d}\cos\theta}$ the IBD cross-section[38] and R is the detector response function. The overall normalization factor C includes the number of free target protons N_p, the live time and the IBD selection efficiencies.

N_p was determined from the total LS volume, density and hydrogen mass fraction, using a geometric survey of the acrylic vessel, flow monitoring during filling and dedicated elemental analyses of LS samples. Combining these measurements yielded $N_p = (1.442 \pm 0.014) \times 10^{33}$.

For each core r, the source spectrum is

$$S_r(E_{\bar{\nu}_e}) = N_f^r [S_{\mathrm{MI}}(E_{\bar{\nu}_e}) + \Delta S_r(E_{\bar{\nu}_e})], \quad (3)$$

where N_f^r is the total number of fissions, derived from the reactor thermal power, fission fractions and energy per fission[99]. The term S_{MI} is a component common to JUNO and Daya Bay and is parameterized in a segmented, largely model-independent (MI) form,

$$S_{\mathrm{MI}}(E_{\bar{\nu}_e}) = S_0(E_{\bar{\nu}_e}) + \sum_{i=1}^{N} \alpha_i B_i(E_{\bar{\nu}_e}), \quad (4)$$

where S_0 is a smooth reference spectrum, B_i are basis functions localized in the ith neutrino energy bin, allowing local deviations from the reference shape; the coefficients α_i are free parameters constrained by the Daya Bay measurement; $N = 25$ defines the granularity of the parameterizatoin, that is, how many segments are allowed for reactor neutrino flux variations in the fit. This construction allowed the combined JUNO and Daya Bay fit to absorb most uncertainties in the absolute reactor spectrum into $\{\alpha_i\}$, whereas JUNO remained primarily sensitive to the oscillatory distortions governed by Δm^2_{21} and $\sin^2\theta_{12}$.

The residual term ΔS_r accounts for differences between individual reactors and the Daya Bay configuration, including small changes in effective fission fractions, contributions from spent nuclear fuel (SNF) and non-equilibrium corrections for long-lived fission fragments[49,87]. The SNF contribution was calculated using the refuelling history and SNF inventory provided by the nuclear power plants, including the shutdown effect[100]. Reactor thermal power, fission fractions and fission energies were taken from standard reactor simulations[99,101–103], with uncertainties at the few-per-mille to per cent level. SNF and non-equilibrium corrections are assigned 30% relative uncertainties but contribute only at the sub-percent level to the total flux. Differences in effective fission fractions between the JUNO and Daya Bay data sets were below 1%, implying that the relative flux normalization between the two experiments is known at about 0.1% level for a 10% uncertainty in the isotopic reference spectra.

Uncertainties in thermal power, fission fractions, SNF and non-equilibrium effects were treated as correlated among cores within the same power plant and uncorrelated between different plants. Extended Data Table 1 summarizes the uncertainties in the predicted non-oscillated antineutrino signal, which serve as inputs for the calculated $\bar{\nu}_e$ rates in Table 1. The resulting time evolution of the predicted IBD rate, compared to the measured rate with backgrounds subtracted, is shown in Extended Data Fig. 6; the observed variations closely track the known reactor power history.

Statistical methods

The first 59.1 days of JUNO data were analysed with a semi-model-independent strategy that combines the prompt-energy spectrum of JUNO with reactor antineutrino measurements from Daya Bay[46,47,104] and state-of-the-art reactor flux calculations[105–107]. A segmented spectral function (equation (4)) was used in the prediction $\mu(\mathbf{p}, \boldsymbol{\eta}, \boldsymbol{\alpha})$ (equation (2)) and shared between JUNO and Daya Bay, so that Daya Bay data

anchored the overall normalization and coarse spectral shape, whereas JUNO was primarily sensitive to the fine oscillation pattern. Summation-based reactor flux models provided the underlying spectral shape and its theoretical uncertainty at the level of $\mathcal{O}(10–20\%)$.

Oscillation parameters were obtained in a frequentist fit using a binned χ^2 function constructed according to the Combined Neyman–Pearson (CNP) method[51]:

$$\chi^2(\mathbf{p},\boldsymbol{\eta},\boldsymbol{\alpha}) = (\mu - D)^T V^{-1}(\mu - D) + \lambda^2_{\text{nuis}}(\boldsymbol{\eta}) + \lambda^2_{\text{flux}}(\boldsymbol{\alpha}) + \chi^2_{\text{osc}}(\sin^2\theta_{13}, \Delta m^2_{31}), \quad (5)$$

where D is the observed IBD prompt-energy spectrum and V is the total covariance matrix. The CNP prescription defines the bin-wise statistical variance in V in a way that reduces known biases of traditional χ^2 definitions for Poisson data. The vector $\mathbf{p}$ contains the oscillation parameters of interest, $\boldsymbol{\eta}$ denotes nuisance parameters describing detector response, backgrounds and overall flux normalization. To ensure a rigorous treatment of external inputs, we distinguish between the data sources used for flux and oscillation constraints. The reactor antineutrino flux (rate and spectral shape) is constrained by a simultaneous fit to the data from the Daya Bay near detectors, whereas the constraints on Δm^2_{31} and $\sin^2\theta_{13}$ are derived predominantly from the near-far relative measurements in ref. 41, without directly incorporating the underlying raw spectral data. Accordingly, the term incorporated the corresponding flux constraints from the Daya Bay near-detector data by directly using the inputs from refs. 46,104, which included the data, the detector response and the covariance matrix describing the measurement uncertainties. An independent analysis constrained the reactor flux by employing $\lambda^2_{\text{flux}}(\boldsymbol{\alpha})$ with nuisance terms as implemented in ref. 47, achieving virtually identical results. The parameter $\boldsymbol{\alpha}$ is defined in equation (4). The term χ^2_{osc} incorporates the published Daya Bay constraints on $\sin^2\theta_{13}$ and Δm^2_{31} (ref. 41) to lift the intrinsic degeneracy in Δm^2_{31} rather than to fix their values. This is achieved using two separate one-dimensional penalty terms, an approach warranted by the negligible correlation between the parameters.

The residual dependence on reactor flux modelling was quantified by constructing a nominal summation model based on the latest nuclear databases and generating an ensemble of alternative spectra that encode plausible fine structures. These spectra were propagated through ensembles of toy data and analysed with the same fit. The additional model-dependent uncertainty on Δm^2_{21} and $\sin^2\theta_{12}$ was below 0.3% after optimizing the segmentation of the spectral function, and was negligible compared with the current total uncertainties.

Three independent analysis chains implemented this framework with different treatments of V, spanning statistically dominated to fully correlated systematic descriptions, and yielded mutually consistent results. Confidence regions in the $(\sin^2\theta_{12}, \Delta m^2_{21})$ plane were obtained from iso-$\Delta\chi^2$ contours at 1σ, 2σ and 3σ levels. A toy Monte Carlo analysis based on the Feldman–Cousins approach[108] has been used to validate the applicability of Wilks's theorem and assess the accuracy of the iso-$\Delta\chi^2$ contours. The distribution of nuisance-parameter pulls shown in Extended Data Fig. 7 represents the largest deviations from nominal values among the common parameters most strongly correlated with the fitted solar neutrino oscillation parameters, illustrating the stability of the fit and the agreement among the three analyses.

Data availability

Raw experimental data from the JUNO detectors are not publicly accessible due to their complexity and volume. Source data for Figs. 3, 4, and Extended Data Fig. 2 are, however, provided. Furthermore, inquiries regarding the data and posteriors used in this result may be directed to the collaboration.

Code availability

The JUNO Collaboration develops and maintains the code used for the simulation of the experimental apparatus and statistical analysis of the raw data used in this result. This code is shared among the Collaboration, but because of the size and complexity of the codebases, it is not publicly distributed. Inquiries regarding the algorithms and methods used in this result may be directed to the Collaboration.

56. Adamson, P. et al. Precision constraints for three-flavor neutrino oscillations from the full MINOS+ and MINOS dataset. *Phys. Rev. Lett.* **125**, 131802 (2020).
57. Wester, T. et al. Atmospheric neutrino oscillation analysis with neutron tagging and an expanded fiducial volume in Super-Kamiokande I–V. *Phys. Rev. D* **109**, 072014 (2024).
58. Abbasi, R. et al. Measurement of atmospheric neutrino oscillation parameters using convolutional neural networks with 9.3 years of data in IceCube DeepCore. *Phys. Rev. Lett.* **134**, 091801 (2025).
59. Abe, K. et al. First joint oscillation analysis of Super-Kamiokande atmospheric and T2K accelerator neutrino data. *Phys. Rev. Lett.* **134**, 011801 (2025).
60. The KM3NeT Collaboration. Measurement of neutrino oscillation parameters with the first six detection units of KM3NeT/ORCA. *J. High Energ. Phys.* **10**, 206 (2024).
61. Abe, K. et al. Results from the T2K experiment on neutrino mixing including a new far detector μ-like sample. *Phys. Rev. Lett.* **135**, 261801 (2025).
62. Abubakar, S. et al. Precision measurement of neutrino oscillation parameters with 10 years of data from the NOvA experiment. *Phys. Rev. Lett.* **136**, 011802 (2026).
63. The NOvA Collaboration & The T2K Collaboration. Joint neutrino oscillation analysis from the T2K and NOvA experiments. *Nature* **646**, 818–824 (2025).
64. Jeon, S. et al. Measurement of reactor antineutrino oscillation parameters using the full 3800-day dataset of the RENO experiment. *Phys. Rev. D* **111**, 112006 (2025).
65. The Double Chooz Collaboration. Double Chooz θ_{13} measurement via total neutron capture detection. *Nat. Phys.* **16**, 558–564 (2020).
66. Acero, M. A. et al. Improved measurement of neutrino oscillation parameters by the NOvA experiment. *Phys. Rev. D* **106**, 032004 (2022).
67. Abe, K. et al. Measurements of neutrino oscillation parameters from the T2K experiment using 3.6×10^{21} protons on target. *Eur. Phys. J C. Part Fields* **83**, 782 (2023).
68. An, F. P. et al. Measurement of electron antineutrino oscillation amplitude and frequency via neutron capture on hydrogen at Daya Bay. *Phys. Rev. Lett.* **133**, 151801 (2024).
69. Wolfenstein, L. Neutrino oscillations in matter. *Phys. Rev. D* **17**, 2369–2374 (1978).
70. Mikheyev, S. P. & Smirnov, A. Y. Resonance amplification of oscillations in matter and spectroscopy of solar neutrinos. *Sov. J. Nucl. Phys.* **42**, 913–917 (1985).
71. Li, Y.-F., Wang, A., Xu, Y. & Zhu, J. Terrestrial matter effects on reactor antineutrino oscillations: constant vs. fluctuated density profiles. *J. High Energ. Phys.* https://doi.org/10.1007/JHEP03(2026)264 (2026).
72. Abusleme, A. et al. Optimization of the JUNO liquid scintillator composition using a Daya Bay antineutrino detector. *Nucl. Instrum. Methods Phys. Res. A* **988**, 164823 (2021).
73. Zhang, Y., Yu, Z. Y., Li, X. Y., Deng, Z. Y. & Wen, L. J. A complete optical model for liquid-scintillator detectors. *Nucl. Instrum. Methods Phys. Res. A* **967**, 163860 (2020).
74. Acquafredda, R. et al. The OPERA experiment in the CERN to Gran Sasso neutrino beam. *J. Instrum.* **4**, P04018 (2009).
75. Abusleme, A. et al. The JUNO experiment top tracker. *Nucl. Instrum. Methods Phys. Res. A* **1057**, 168680 (2023).
76. Abusleme, A. et al. The design and sensitivity of JUNO's scintillator radiopurity pre-detector OSIRIS. *Eur. Phys. J. C.* **81**, 973 (2021).
77. The JUNO Collaboration. Radioactivity control strategy for the JUNO detector. *J. High Energ. Phys.* **2021**, 102 (2021).
78. Huang, G.-H., Jiang, W., Wen, L.-J., Wang, Y.-F. & Luo, W.-M. Data-driven simultaneous vertex and energy reconstruction for large liquid scintillator detectors. *Nucl. Sci. Tech.* **34**, 83 (2023).
79. Liu, Q., He, M., Ding, X., Li, W. & Peng, H. A vertex reconstruction algorithm in the central detector of JUNO. *J. Instrum.* **13**, T09005 (2018).
80. Takenaka, A. et al. Neutron source-based event reconstruction algorithm in large liquid scintillator detectors. *Eur. Phys. J. C* **85**, 1097 (2025).
81. Berger, M. J., Coursey, J. S., Zucker, M. A. & Chang, J. *ESTAR, PSTAR and ASTAR: Computer Programs for Calculating Stopping-Power and Rrange Tables for Electrons, Protons, and Helium Ions* (version 1). NIST Standard Reference Database 124 (2017).
82. Birks, J. B. *The Theory and Practice of Scintillation Counting* (Pergamon, 1964).
83. Frank, I. M. & Tamm, I. E. Coherent visible radiation of fast electrons passing through matter. *Compt. Rend. Acad. Sci. URSS* **14**, 109–114 (1937).
84. Agostinelli, S. et al. GEANT4–a simulation toolkit. *Nucl. Instrum. Methods Phys. Res. A* **506**, 250–303 (2003).
85. Battistoni, G. et al. Overview of the FLUKA code. *Ann. Nucl. Energy* **82**, 10–18 (2015).
86. Ahdida, C. et al. New capabilities of the FLUKA multi-purpose code. *Front. Phys.* **9**, 788253 (2022).
87. An, F. P. et al. Measurement of electron antineutrino oscillation based on 1230 days of operation of the Daya Bay experiment. *Phys. Rev. D* **95**, 072006 (2017).
88. Strati, V. et al. Expected geoneutrino signal at JUNO. *Prog. Earth Planet. Sci.* **2**, 5 (2015).
89. Reguzzoni, M. et al. GIGJ: a crustal gravity model of the Guangdong province for predicting the geoneutrino signal at the JUNO experiment. *J. Geophys. Res. Solid Earth* **124**, 4231–4249 (2019).
90. Gao, R. et al. JULOC: a local 3-D high-resolution crustal model in South China for forecasting geoneutrino measurements at JUNO. *Phys. Earth Planet. Interiors* **299**, 106409 (2020).
91. Han, R. et al. Expected geoneutrino signal at JUNO using local integrated 3-D refined crustal model. Preprint at https://arxiv.org/abs/2210.09165 (2022).

92. Agostini, M. et al. Comprehensive geoneutrino analysis with Borexino. *Phys. Rev. D* **101**, 012009 (2020).
93. Cheng, J. et al. Neutral-current background induced by atmospheric neutrinos at large liquid-scintillator detectors: III. Comprehensive prediction for low energy neutrinos. *Eur. Phys. J. C* **85**, 295 (2025).
94. Andreopoulos, C. et al. The GENIE neutrino Monte Carlo generator. *Nucl. Instrum. Meth. Phys. Res. A* **614**, 87–104 (2010).
95. Golan, T., Sobczyk, J. T. & Zmuda, J. NuWro: the Wroclaw Monte Carlo generator of neutrino interactions. *Nucl. Phys. B Proc. Suppl.* **229-232**, 499 (2012).
96. Honda, M., Sajjad Athar, M., Kajita, T., Kasahara, K. & Midorikawa, S. Atmospheric neutrino flux calculation using the NRLMSISE-00 atmospheric model. *Phys. Rev. D* **92**, 023004 (2015).
97. Koning, A. J., Hilaire, S. & Duijvestijn, M. C. TALYS: comprehensive nuclear reaction modeling. *AIP Conf. Proc.* **769**, 1154–1159 (2005).
98. JUNO Collaboration. Simulation of the background from $^{13}C(\alpha,n)^{16}O$ reaction in the JUNO scintillator. *Eur. Phys. J. C* **85**, 1080 (2025).
99. Ma, X. B., Zhong, W. L., Wang, L. Z., Chen, Y. X. & Cao, J. Improved calculation of the energy release in neutron-induced fission. *Phys. Rev. C* **88**, 014605 (2013).
100. Ma, X. B., Zhao, Y. F., Chen, Y. X., Zhong, W. L. & An, F. P. Antineutrino flux and spectrum calculation for spent nuclear fuel for the Daya Bay antineutrino experiment. *Nucl. Phys. A* **966**, 294–305 (2017).
101. Sanchez, R. et al. APOLLO2 year 2010. *Nucl. Eng. Tech.* **42**, 474–499 (2010).
102. Ma, X. B. et al. Uncertainty analysis of fission fraction for reactor antineutrino experiments. *Mod. Phys. Lett. A* **31**, 1650120 (2016).
103. An, F. P. et al. Improved Measurement of the reactor antineutrino flux and spectrum at Daya Bay. *Chin. Phys. C* **41**, 013002 (2017).
104. An, F. P. et al. Antineutrino energy spectrum unfolding based on the Daya Bay measurement and its applications. *Chin. Phys. C* **45**, 073001 (2021).
105. Estienne, M. et al. Updated summation model: an improved agreement with the Daya Bay antineutrino fluxes. *Phys. Rev. Lett.* **123**, 022502 (2019).
106. Fang, D.-L., Li, Y.-F. & Zhang, D. *Ab initio* calculations of reactor antineutrino fluxes with exact lepton wave functions. *Phys. Lett. B* **813**, 136067 (2021).
107. Perissé, L. et al. Comprehensive revision of the summation method for the prediction of reactor $\overline{\nu}_e$ fluxes and spectra. *Phys. Rev. C* **108**, 055501 (2023).
108. Feldman, G. J. & Cousins, R. D. Unified approach to the classical statistical analysis of small signals. *Phys. Rev. D* **57**, 3873–3889 (1998).

Acknowledgements We acknowledge the continued cooperation and support of the China General Nuclear Power Group in the construction and operation of the JUNO experiment. We also recognize the computing resources provided by the Chinese Academy of Sciences, IN2P3, INFN and JINR, which are essential for data processing and analysis within the JUNO Collaboration. We acknowledge the financial and institutional support from the Chinese Academy of Sciences, the National Key R&D Program of China, the People's Government of Guangdong Province, the Tsung–Dao Lee Institute of Shanghai Jiao Tong University, and the China Center of Advanced Science and Technology in China. We appreciate the contributions from the Institut National de Physique Nucléaire et de Physique des Particules (IN2P3) in France, the Istituto Nazionale di Fisica Nucleare (INFN) in Italy, the Fonds de la Recherche Scientifique (F.R.S.–FNRS) and the Institut Interuniversitaire des Sciences Nucléaires (IISN) in Belgium, and the Conselho Nacional de Desenvolvimento Científico e Tecnológico (CNPq) in Brazil. We also acknowledge the support of the Agencia Nacional de Investigación y Desarrollo (ANID) and the ANID–Millennium Science Initiative Program (ICN2019044) in Chile; the European Structural and Investment Funds, the Ministry of Education, Youth and Sports, and the Charles University Research Center in the Czech Republic; the Deutsche Forschungsgemeinschaft (DFG), the Helmholtz Association, and the Cluster of Excellence PRISMA+ in Germany; and the Joint Institute for Nuclear Research (JINR) and Lomonosov Moscow State University in Russia. We further thank the Slovak Research and Development Agency in the Slovak Republic, the National Science and Technology Council (NSCT) and MOE in Taiwan, China, the Program Management Unit for Human Resources and Institutional Development, Research and Innovation (PMU–B), Chulalongkorn University, and Suranaree University of Technology in Thailand, the Science and Technology Facilities Council (STFC) in the United Kingdom, and the University of California at Irvine and the National Science Foundation (NSF) in the United States.

Author contributions The JUNO detector was designed, constructed, commissioned and is being operated by the JUNO Collaboration. All aspects of the hardware and software developments, data taking, detector calibration, data processing, Monte Carlo simulation, as well as data analysis, were performed by JUNO members, who also discussed and approved scientific results. All authors reviewed and approved the final version of the paper.

Competing interests The authors declare no competing interests.

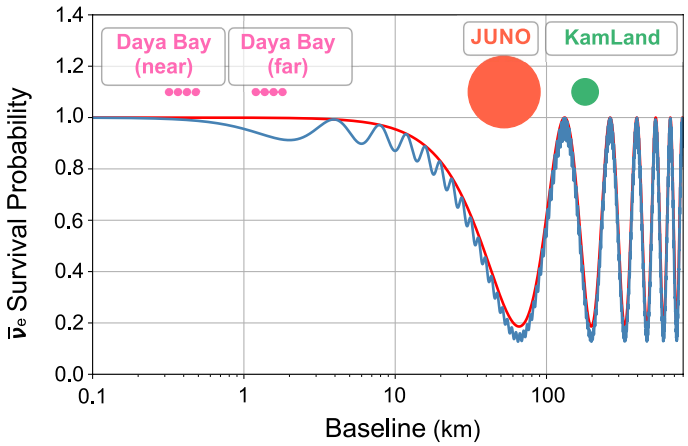
Additional information

Supplementary information The online version contains supplementary material available at https://doi.org/10.1038/s41586-026-10538-z.

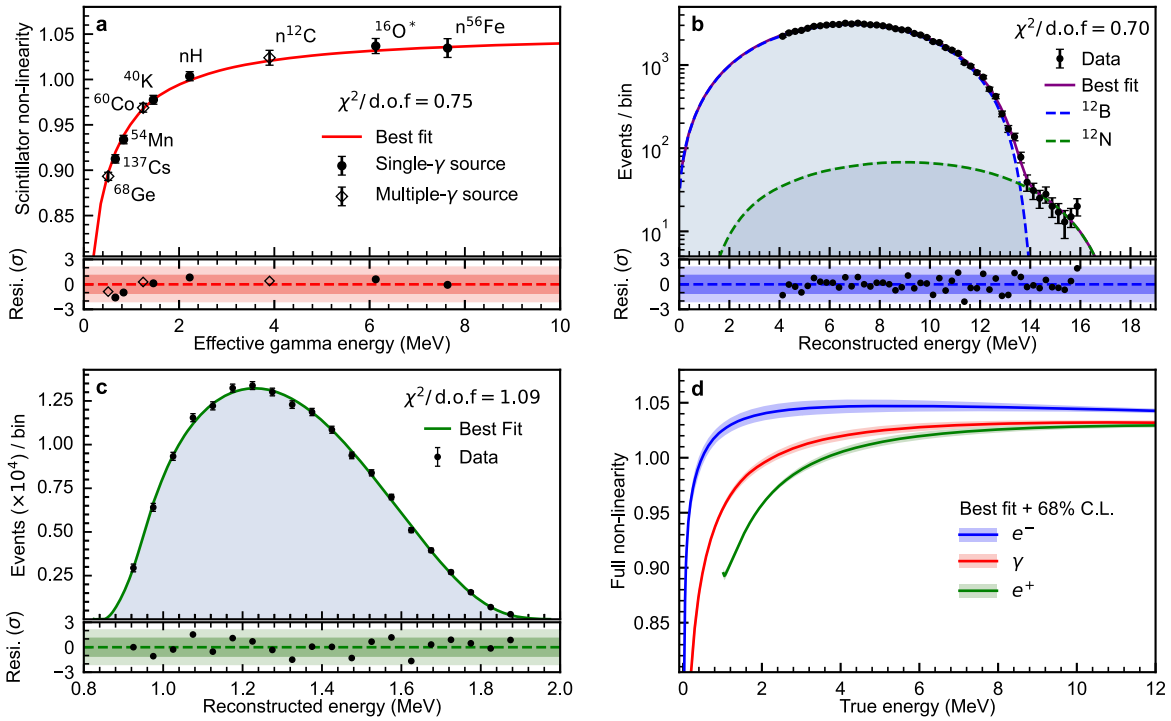
Correspondence and requests for materials should be addressed to The JUNO Collaboration.

Peer review information *Nature* thanks Antonio Marrone, Robert Svoboda, Patricia Vahle, Zoya Vallari and the other, anonymous, reviewer(s) for their contribution to the peer review of this work. Peer reviewer reports are available.

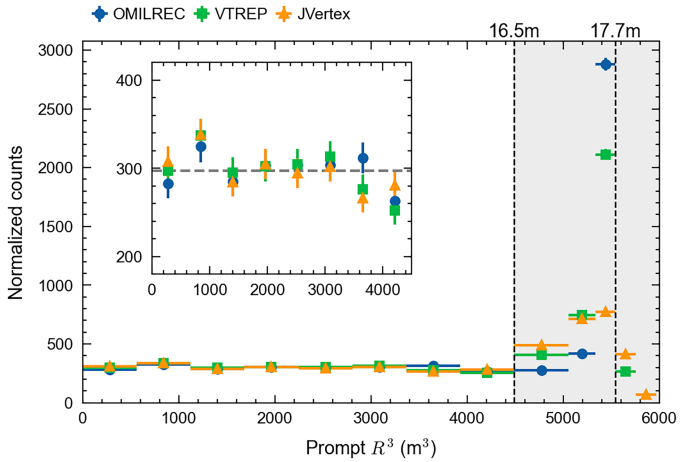
Reprints and permissions information is available at http://www.nature.com/reprints.



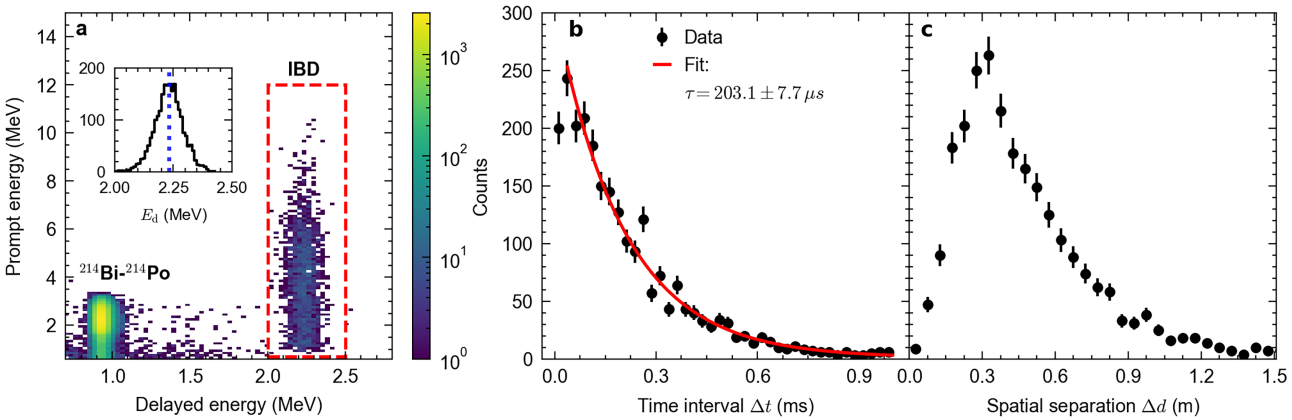
Extended Data Fig. 1 | Reactor neutrino oscillation at different baselines. Survival probability $\mathcal{P}_{ee}$ of 4 MeV reactor $\bar{\nu}_e$ vs. baseline. Red: slow solar oscillation (Δm^2_{21}); blue: total $\mathcal{P}ee$ including fast atmospheric oscillations (Δm^2_{31}). Experimental baselines: JUNO (orange, 52.5 km) near solar oscillation maximum, Daya Bay near/far (pink), KamLAND (green). Circle sizes scale with detector sizes.



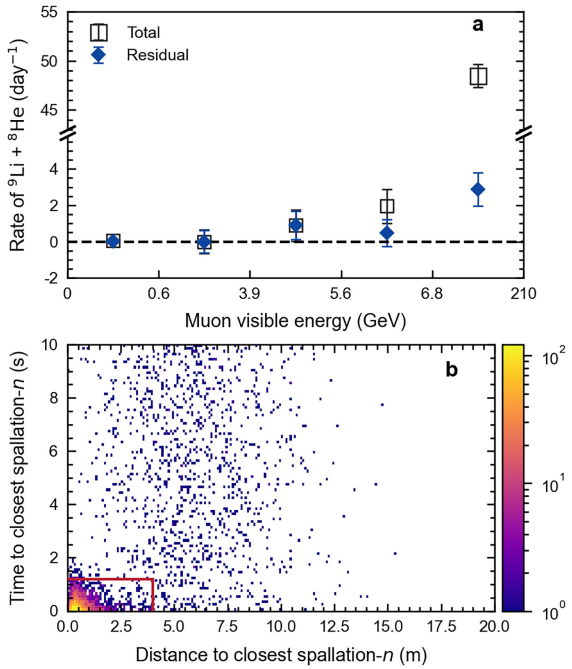
Extended Data Fig. 2 | Energy scale non-linearity calibration. a, Scintillator non-linearity from γ calibration sources deployed at the detector's center: single-γ sources (solid circle), multiple-γ sources (hollow rhombus), and the best-fit curve (red). **b**, Measured cosmogenic ^{12}B β^- spectrum (points) compared to prediction (purple line), with a best-fit ^{12}N component (green dashed line) of 2.7% identified via its high-energy shoulder. **c**, Measured ^{11}C β^+ spectrum (points) and the best-fit model (green line). **d**, Non-linearity response model for electrons (blue), γ's (red), and positrons (green).



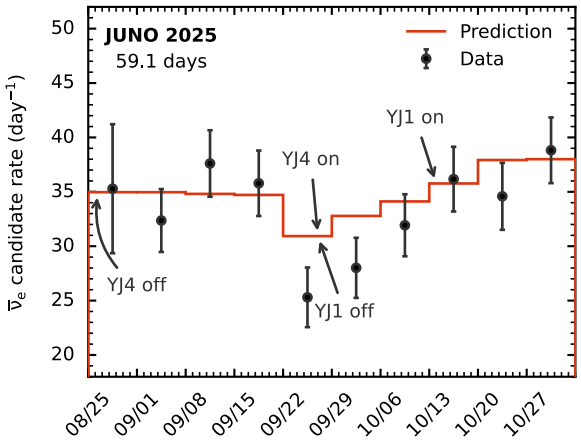
Extended Data Fig. 3 | Spatial distribution of reactor neutrino candidates. Prompt-event counts versus reconstructed cubic radius (R^3) are shown for the three vertex algorithms: OMILREC (blue), VTREP (green), and JVertex (orange). Horizontal bars indicate R^3 bin widths; vertical dashed lines mark the FV boundary (16.5 m) and detector edge (17.7 m). The inset shows the uniform event density within the FV, with the dashed line indicating the mean count level. The rising counts beyond the FV are primarily due to accidental coincidences, with minor contributions from fast- and double-neutron backgrounds.



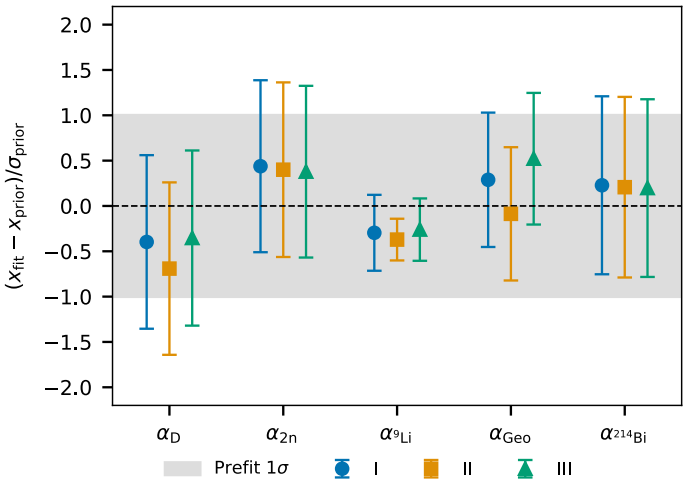
Extended Data Fig. 4 | Reactor neutrino candidates characteristics. **a**, Two-dimensional prompt-versus-delayed energies (with enlarged delayed energy window) showing the ^{214}Bi-^{214}Po cluster at E_d ~ 1 MeV and the IBD selection region (dashed red box). The inset shows the delayed-energy spectrum, featuring a clear neutron-capture peak at $E_d \simeq 2.23$ MeV (blue dashed line). **b**, Temporal correlation following an exponential decay with a fitted neutron-capture time of $\tau = 203.1 \pm 7.7\,\mu$s. The deviation of the first point is due to the $\Delta t > 5\,\mu$s cut and is therefore not included in the fit. **c**, Spatial separation Δd of the prompt and delayed vertices.



Extended Data Fig. 5 | ^{9}Li/^{8}He background analysis. a, Measured ^{9}Li/^{8}He rates across muon visible energy, comparing data before and after the SPN veto. The residual ^{9}Li/^{8}He rates are shown prior to efficiency correction but after the application of all selection cuts. **b**, Spatial- and temporal-distribution of IBD candidates before the SPN cut shown relative to preceding SPN events. A clear cluster of ^{9}Li/^{8}He events is visible at the origin. The red box indicates the SPN veto criteria.



Extended Data Fig. 6 | Temporal distribution of reactor neutrinos. Rates of antineutrino candidates (after subtraction of the mean background rates), shown in one week time bins (black points with statistical error) are compared to the prediction (red line). Arrows indicate operations on the cores YJ1 and YJ4 of the Yangjiang nuclear power plants. The power plants reduced the power output due to the occurrence of Super Typhoon Ragasa on September 24th.



Extended Data Fig. 7 | Three analyses post-fit comparison. Post-fit pulls of selected nuisance parameters in the three independent JUNO analysis chains. From left to right, these parameters correspond to the detection efficiency, the double-neutron rate, the ^{9}Li/^{8}He rate, the geoneutrino rate, and the ^{214}Bi-^{214}Po rate. Coloured markers with vertical error bars show the best-fit shift and 1σ uncertainty of each parameter relative to its prior, $(x_{fit} - x_{prior})/\sigma_{prior}$, for Analyses I–III, while the shaded band denotes the ±1σ prefit range and the dashed line indicates zero pull.

Extended Data Table 1 | Summary of detector and reactor related uncertainties on the predicted reactor neutrino rate

Source	Uncertainties
Target protons	1.0%
Reference spectrum	1.2%
Thermal power	0.5%
Fission fraction	0.6%
Spent nuclear fuel	0.3%
Non-equilibrium	0.2%
Different fission fraction	0.1%